Structural basis for heteromeric assembly and subthreshold activation of human M-channel

Yifei Wang[1,2,3,6], Hui Yang[1,2,3,6], Yannan Qu[1,2,3,6], Junnan Li[4,6], Xiao Li[1,2,3], Wenxin Hou[1], Kun Wu[1], Guanglei Xie[1,2,3], Xi Wang[1,2,3], Yangliang Ye[5], Huaiyu Yang[4,7], and Huaizong Shen[1,2,3,7]

[1]Zhejiang Key Laboratory of Structural Biology, School of Life Sciences, Westlake University, Hangzhou, Zhejiang, China

[2]Westlake Laboratory of Life Sciences and Biomedicine, Hangzhou, Zhejiang, China

[3]Westlake Institute for Advanced Study, Hangzhou, Zhejiang, China

[4]Shanghai Key Laboratory of Regulatory Biology, Institute of Biomedical Sciences and School of Life Sciences, East China Normal University, Shanghai, China

[5]Suzhou Institute of Materia Medica, Suzhou, Jiangsu, China

[6]These authors contributed equally

[7]To whom correspondence should be addressed: H. Yang (hyyang@bio.ecnu.edu.cn); H. Shen (shenhuaizong@westlake.edu.cn).

Abstract

The M-channel, a heterotetrameric voltage-gated potassium channel formed by KCNQ2 and KCNQ3 subunits, critically regulates neuronal excitability, with dysfunction linked to epilepsy and developmental encephalopathies. Despite its physiological importance, structural mechanisms governing its unique heteromeric assembly and subthreshold gating have remained unresolved. We present cryo-EM structures of human M-channels revealing unprecedented stoichiometric plasticity, with all possible KCNQ2:KCNQ3 configurations (1:3 to 3:1) observed. Electrophysiology of engineered concatemers shows these assemblies recapitulate native function. Structural analyses uncover that KCNQ3's voltage-sensing domain (VSD) adopts a more depolarized conformation than KCNQ2, explaining its signature subthreshold activation. Leveraging these insights, we developed CLM142, a structure-guided activator with 10-fold greater potency and specificity than withdrawn retigabine. CLM142 enabled open-state structure determination, revealing how PIP_2 binding couples VSD movement to pore opening. Our work provides an atomic-resolution framework for understanding M-channel's unique assembly, physiology, disease mechanisms, and targeted therapeutic design.

The M-channel, a heteromeric voltage-gated potassium (K_v) channel composed of KCNQ2 and KCNQ3 subunits (*1-3*), governs neuronal excitability by generating a slowly activating, non-inactivating potassium current (I_M) that dampens repetitive firing (*2, 4-6*). First identified in sympathetic neurons for its suppression by muscarinic acetylcholine receptor signaling (hence "M"-channel) (*4*), it is now recognized as a master regulator of action potential threshold and spike-frequency adaptation across the central and peripheral nervous systems (*6-12*). The molecular identity of I_M was established with the cloning of *KCNQ2* and *KCNQ3* (*1, 2, 13-16*), which form heteromeric channels with biophysical properties precisely matching native M-currents—distinct from their homomeric counterparts (*2, 3, 17, 18*). Dysfunction of these subunits underlies a spectrum of severe neurological disorders, including benign familial neonatal seizures (BFNS) (*3, 5, 13, 15, 19-29*), developmental epileptic encephalopathies (DEE7) (*23, 30-33*), and autism-associated phenotypes (*34-37*), underscoring their critical physiological and therapeutic relevance (*38*).

Despite decades of research, fundamental questions regarding the M-channel's architecture and gating mechanisms remain unresolved (*36, 39*). A central controversy concerns its heteromeric stoichiometry (*36*): while biochemical and functional studies suggested a 2:2 (KCNQ2:KCNQ3) assembly (*2, 40*), others proposed variable or asymmetric arrangements (*41, 42*). This uncertainty has obscured how subunit composition dictates the channel's unique subthreshold activation—a hallmark feature enabling I_M to stabilize resting membrane potentials (*2, 4, 6*). Although recent structures of homomeric KCNQ channels have revealed their canonical architecture (*39, 43-48*), the absence of

heteromeric M-channel structures has precluded mechanistic understanding of its distinct gating properties and subunit cooperativity (*36, 49, 50*). Resolving these questions is critical for both ion channel biology and drug discovery, particularly given the M-channel's validation as a target for epilepsy and neuropsychiatric disorders (*49, 51-54*).

Therapeutic targeting of the M-channel has faced significant hurdles (*51, 55*). Retigabine, the first-in-class M-channel activator approved for refractory epilepsy was withdrawn due to dose-limiting off-target effects (e.g., bladder toxicity and retinal discoloration) linked to its activity across multiple KCNQ subtypes (*53, 54, 56-61*). Developing subtype-selective activators requires precise structural insights into the heteromeric channel’s drug-binding sites and activation mechanisms—a goal hindered by the lack of M-channel structures.

Here, we resolve these longstanding questions through cryo-electron microscopy (cryo-EM) structures of the human M-channel in multiple functional states. Our findings reveal unexpected stoichiometric flexibility in KCNQ2:KCNQ3 assemblies and identify a markedly depolarized conformation of the voltage-sensing domain (VSD) in KCNQ3 compared to KCNQ2, providing the first structural explanation for the channel's characteristic subthreshold activation. Electrophysiological characterizations of engineered concatemers and chimeric constructs corroborate these structural insights. Leveraging this knowledge, we developed CLM142 (**1**), a potent and selective M-channel activator that enabled determination of the open-state structure. Our work not only elucidates

fundamental principles of M-channel assembly and gating but also establishes a framework for structure-guided development of targeted therapies.

Structure of the human M-channel reveals unexpected stoichiometric plasticity

We determined cryo-EM structures of the human M-channel using both wild-type KCNQ2/KCNQ3 heteromers and engineered constructs where flexible N- and C-terminal regions and the disordered loop between HA and HB helices were removed to improve biochemical stability (Fig. 1A, figs. S1 to S11, and Tables S1 to S5). This approach enabled us to resolve four distinct structural states: the wild-type M-channel (M-channel^{WT}; Fig. 1A), engineered constructs without ligands (M-channel^{apo}; fig. S3A), constructs bound to the activator CLM142 (M-channel^{CLM142}; fig. S3B), and constructs with both CLM142 and phosphatidylinositol 4,5-bisphosphate (PIP_2) to stabilize the open state (M-channel^{open}; fig. S3C).

Analysis of these preparations revealed the M-channel exists in four distinct stoichiometric configurations (Fig. 1A and fig. S3). These include a 3:1 KCNQ2:KCNQ3 assembly (M2223), two 2:2 assemblies with either adjacent (M2233) or alternating (M2323) subunit arrangements, and a 1:3 assembly (M2333). Intriguingly, the relative proportions of these assemblies varied significantly between preparations. Under our standard co-expression conditions for wild-type subunits, the KCNQ2-rich M2223 configuration was the least prevalent (6.45%), indicating an inherent assembly preference under these conditions that favors incorporation of KCNQ3. This resulted in a population dominated by the balanced 2:2 stoichiometries (M2323, 38.38%; M2233, 32.6%) and the

KCNQ3-rich M2333 configuration (22.57%) (Fig. 1A). In contrast, engineered constructs exhibited a pronounced redistribution, with the M2223 configuration becoming dominant (53.2% in M-channel^{apo}) (fig. S3), correlating with higher expression levels of KCNQ2 relative to KCNQ3 (fig. S2B).

This stoichiometric plasticity was further quantified through systematic transfection experiments using defined KCNQ2-GFP:KCNQ3 plasmid ratios (1:1, 1:4, and 1:9), which showed that the ratio of GFP fluorescence (reporting KCNQ2 incorporation) to total protein yield (UV absorbance) decreased progressively (146, 128, and 54 mV/mAu, respectively) with reduced KCNQ2 plasmid input (fig. S12). Together, these data demonstrate that the observed stoichiometric flexibility is an inherent property of M-channel assembly—at least in our heterologous expression system—and that the final population distribution is a direct consequence of the relative expression levels of the constituent subunits within the heterologous system.

All resolved structures adopted the canonical voltage-gated K^+ channel architecture, with four voltage-sensing domains (VSDs) surrounding a central pore domain (PD; Fig. 1, B and C) (*62*). However, unlike homomeric channels, the M-channel's central pore and VSDs are formed by asymmetric arrangements of KCNQ2 and KCNQ3 subunits (*39, 43-46, 48*). Three key structural features enabled unambiguous discrimination between subunits: first, the VSD of KCNQ3 adopts a distinct orientation relative to the central pore compared to KCNQ2 (Fig. 1, D and E); second, KCNQ3 possesses a significantly longer extracellular loop (ECL) which yields a pronounced density difference (Fig. 1F and fig.

S1); and third, the high resolution (~2.8 Å) of the central pore region allowed discrimination of non-conserved residues, including Y284 in KCNQ2 versus T323 in KCNQ3, F316 in KCNQ2 versus L355 in KCNQ3, and Y226 in KCNQ2 versus C255 in KCNQ3 (Fig. 1G and fig. S1).

The high-resolution structure enables precise structural alignment of the subunit interface (S5 and S6 helices) of KCNQ2 and KCNQ3, revealing an exceptional degree of conservation in both sequence (>90% similarity) and tertiary structure (RMSD = 0.437 Å; fig. S13). This near-perfect structural compatibility explains the M-channel's remarkable stoichiometric plasticity, permitting all combinatorially possible configurations (M2223, M2233, M2323, and M2333) to assemble with comparable thermodynamic stability. Crucially, this structural degeneracy establishes an expression-level-dependent assembly paradigm, where the relative abundances of distinct configurations are principally determined by the relative availability of constituent subunits rather than preferential binding affinities.

Concatemeric constructs of KCNQ2 and KCNQ3 recapitulate electrophysiological properties of the wild-type M-channel

To validate the physiological relevance of the observed stoichiometric assemblies, we engineered concatemers with defined subunit ratios matching our structural findings: 3:1 (M2223), two distinct 2:2 arrangements (M2323 and M2233), and 1:3 (M2333) (Fig. 2B). These constructs enabled precise control over subunit composition while maintaining native inter-domain connectivity.

159

160 We performed comprehensive electrophysiological characterization using both
161 whole-cell and single-channel recordings (Fig. 2). Wild-type M-channels (co-expressed
162 KCNQ2/KCNQ3) served as functional benchmarks (Fig. 2, A and C), while KCNQ2
163 homomers provided baseline references for homomeric channel properties (Fig. 2C).
164 Whole-cell recordings demonstrated that all four concatemer configurations produced
165 current-voltage (I-V) relationships superimposable with wild-type M-channels, with
166 activation thresholds consistently shifted toward hyperpolarized potentials compared to
167 KCNQ2 homomers (Fig. 2C). Quantitative analysis revealed that each concatemer
168 exhibited half-maximal activation voltages ($V_{1/2}$) statistically indistinguishable from wild-
169 type M-channels ($p > 0.05$) yet significantly more hyperpolarized than KCNQ2 homomers
170 ($p < 0.001$), recapitulating the hallmark sub-threshold activation profile of native M-
171 channels (*2*).

172

173 Single-channel analyses provided mechanistic corroboration at the molecular level.
174 All concatemer variants displayed unitary current amplitudes (Fig. 2E), single-channel
175 conductance (Fig. 2F), and open probabilities (Fig. 2G) matching wild-type M-channels
176 within experimental error ($p > 0.05$ for all parameters across constructs). This functional
177 equivalence across distinct stoichiometries demonstrates that each assembly configuration
178 faithfully reproduces the fundamental biophysical properties of native M-channels (*63*).

179

180 **The KCNQ3 voltage-sensing domain confers hyperpolarized activation kinetics**

The M-channel's physiological importance stems from its unique ability to activate at subthreshold membrane potentials, a property critical for regulating neuronal excitability (*2, 4, 6*). Despite its functional significance, the structural basis for this distinctive gating behavior has remained elusive.

In voltage-gated ion channels, VSD activation is defined by the positions of S4 arginine residues (R1-R6) relative to the charge transfer center (CTC), which comprises a conserved phenylalanine (F137 in KCNQ2; F167 in KCNQ3) flanked by two acidic residues (E130/E140 in KCNQ2; E160/E170 in KCNQ3; Fig. 3A and fig. S1) (*64*). Comparative structural analysis of M-channel^{apo} revealed striking differences between subunits: while R4 (R207) in KCNQ2 forms cation-π interactions with F137 and sits slightly above it, KCNQ3's R4 (R236) resides farther above F167, with R5 (R239) instead forming the cation-π interaction below (Fig. 3A). This conformational disparity indicates that KCNQ3's VSD favors the activated state at more hyperpolarized potentials than KCNQ2, suggesting its VSD requires less depolarization to activate. These structural observations provide a plausible mechanism for the M-channel's hyperpolarized activation threshold relative to KCNQ2 homomers.

To test whether KCNQ3's VSD drives subthreshold activation, we engineered chimeric constructs by swapping VSDs between subunits: VSD_2-PD_3 (KCNQ2 VSD + KCNQ3 pore) and VSD_3-PD_2 (KCNQ3 VSD + KCNQ2 pore) (Fig. 3B and fig. S1). Electrophysiological characterization revealed that channels containing only KCNQ2 VSDs (VSD_2-PD_3 + KCNQ2) exhibited activation thresholds similar to KCNQ2 homomers

(Figures 3C and 3D). Conversely, channels with exclusively KCNQ3 VSDs (VSD_3-PD_2 + KCNQ3) activated at even more hyperpolarized potentials than wild-type M-channels, with the native heteromer's threshold intermediate between these extremes (Fig. 3, C and D). These results definitively establish that KCNQ3's VSD is both necessary and sufficient for the M-channel's subthreshold activation phenotype.

Molecular mechanism for the potent activation of CLM142 on human M-channel

The withdrawal of retigabine (Fig. 4B), the first clinically approved M-channel activator, due to off-target effects across KCNQ subtypes (fig. S15), highlighted the critical need for selective therapeutics (*49, 51, 53, 54, 56-61*). Through structure-guided drug design informed by both the M-channel architecture and retigabine's activation mechanism, we developed CLM142 (**1**; Fig. 4A), a next-generation activator identified via an integrated virtual screening and electrophysiological validation approach.

CLM142 features three key structural elements: (1) a fluorophenyl group linked via (2) an amide bond to (3) an indazole core with cyclopropyl and ethynyl substitutions (Fig. 4A). These strategic modifications yielded significant pharmacological improvements, demonstrating a 10-fold greater potency than retigabine on human M-channel (EC_{50} = 0.19 ± 0.09 μM versus 2.16 ± 0.15 μM for G-V curve shifts) while achieving an enhanced subtype specificity, as evidenced by its negligible effects on KCNQ4 channel (Fig. 4, C to G, and fig. S14A). At 1 μM concentration, CLM142 produced a $\Delta V_{1/2}$ shift of -32.49 ± 1.64 mV (Fig. 4, C and D) and significantly modulated channel kinetics, accelerating activation (118.09 ± 9.21 ms versus 172.09 ± 17.19 ms at 0 mV; fig. S14B) while slowing

227 deactivation (126.54 ± 12.98 ms versus 19.51 ± 2.72 ms; fig. S14C). These properties
228 establish CLM142 as a promising therapeutic candidate combining submicromolar potency
229 with improved selectivity for human M-channel.
230
231 To elucidate its mechanism of action, we determined the cryo-EM structure of M-
232 channel^{CLM142} at 3.1 Å resolution (Fig. 5, A and B, and figs. S3, S4, and S10). CLM142
233 occupies the inter-subunit pocket between S5 and S6 helices (Fig. 5C) - the canonical
234 activator binding site shared with retigabine (fig. S15) - but establishes a unique interaction
235 network through its distinct chemical architecture (Fig. 5D) (*39, 45*). The compound binds
236 in a characteristic orientation where its fluorophenyl group extends intracellularly while the
237 cyclopropyl/ethynyl moieties project extracellularly, creating extensive interactions (Fig.
238 5D). The amide carbonyl forms a crucial hydrogen bond with S303/S342 on S6, while the
239 central indazole core engages in π-π stacking with the highly conserved W236/W265 on S5.
240 Simultaneously, the cyclopropyl/ethynyl groups are positioned within a hydrophobic pocket
241 formed by F240/F269 on S5 and L299/L338-F305/F344 on S6, while the fluorophenyl
242 group makes complementary van der Waals contacts with F304/F343, L221/L250,
243 V225/I254 and L312/L352. This sophisticated interplay of directional hydrogen bonding
244 and extensive hydrophobic complementarity synergistically enables CLM142 to bind and
245 activate M-channel.
246
247 Despite dramatical modifications, CLM142 activates the channel through a similar
248 mechanism to retigabine, promoting pore domain opening by displacing S5 and S6 helices
249 in a clockwise rotation (viewed from intracellular side; Fig. 5D) (*39, 45, 65*). This

movement is evidenced by significant displacement of W236 in KCNQ2/W265 in KCNQ3 on S5 (Fig. 5D), confirming that both compounds share a common activation pathway despite their distinct binding geometries.

Open-state structure of M-channel reveals its activation mechanism

To elucidate the structural basis of M-channel activation, we determined the open-state structure of the human M-channel (M-channel^{open}) in complex with CLM142 and PIP_2 (Fig. 6, A and B, figs. S3, S4, and S11). While maintaining the four CLM142 molecules bound between S5-S6 helices observed in the closed state (Fig. 6B), the intracellular gate formed by L318 in KCNQ2 (L357 in KCNQ3) of the open structure undergoes significant dilation, expanding from less than 1 Å to over 2 Å in radius (Fig. 6, C and D). This pore opening results from a coordinated clockwise rotation of S6 helices (viewed intracellularly) initiated at the conserved G313 in KCNQ2 (G352 in KCNQ3) within the GSG motif, coupled with outward displacement of the gate-forming leucine side chains (L318/L357) (Fig. 6E and figs. S1 and S16). These movements align with established activation mechanisms in voltage-gated channels (*45, 65*).

The structure captures four weak densities beneath the VSDs, which we assign as PIP_2 based on three lines of evidence (Fig. 6F): (i) their exclusive appearance in PIP_2-supplemented samples, (ii) the open conformation's dependence on PIP_2 in KCNQ channels (*50, 66-69*), and (iii) congruence with PIP_2 binding sites in other open-state KCNQ structures (*39, 44, 46-48, 70*). These lipids engage multiple positively charged residues, including R87/R117 and R89/R119 in the VSD, R213/R242 and R214/R243 in the S4-S5

linker, and K327/K366 in the extended S6 helix through electrostatic interactions, consistent with previous studies (*44, 46-48*). These interactions support an activation mechanism whereby PIP_2 binding to this basic residue-rich interface couples S4 movement to S6 displacement, facilitating gate opening. The pivotal role of the conserved GSG motif (G313/G352) as a gating hinge is underscored by its position at the initiation point of these conformational changes (fig. S1).

Discussion

Our systematic structural and functional characterization of the human M-channel resolves several long-standing questions in the field while providing new insights into its physiological regulation, pathophysiological mechanism and therapeutic targeting (fig. S17).

Our cryo-EM structures reveal unexpected stoichiometric plasticity in the M-channel, which can adopt all possible KCNQ2:KCNQ3 configurations (M2223, M2233, M2323, and M2333). This remarkable structural flexibility likely stems from the high degree of sequence conservation and structural similarity between KCNQ2 and KCNQ3 subunits. The relative abundance of these assemblies varies across preparations, correlating with differential expression levels of KCNQ2 and KCNQ3. This structural flexibility resolves previous conflicting reports about M-channel composition, where some studies proposed fixed 1:1 stoichiometry while others suggested variable ratios (*2, 40-42*). The discrepancy likely stems from unaccounted variations in subunit expression levels across experimental systems.

This plasticity may represent an important endogenous mechanism for tuning neuronal excitability, particularly given the established spatiotemporal expression patterns of KCNQ subunits (*12, 16, 71-73*). During development, KCNQ2 expression stabilizes rapidly while KCNQ3 shows gradual accumulation to its peak levels (*16, 71, 72*). Furthermore, distinct brain regions exhibit characteristic KCNQ2/KCNQ3 expression ratios (*12, 74, 75*). Such systematic variations in subunit availability would naturally produce different distributions of M-channel assemblies and KCNQ2 homomers, creating a spectrum of channel populations fine-tuned to specific physiological requirements across neuronal circuits and developmental stages.

Despite structural heterogeneity, all four configurations exhibited remarkably similar electrophysiological properties. This surprising functional homogeneity may reflect either: (1) dominant activation by the first responsive subunit as proposed previously, or (2) limitations in detecting subtle gating differences with current methodologies (*76*). If confirmed, such functional equivalence would imply that stoichiometric variation primarily modulates channel density rather than biophysical properties—a possibility that warrants further investigation.

Through chimeric constructs and high-resolution structures, we established that KCNQ3's VSD drives the M-channel's characteristic subthreshold activation. While the VSDs of KCNQ2 and KCNQ3 share overall architecture, subtle sequence variations create distinct electrostatic landscapes that alter voltage sensitivity. Future studies mapping these

sequence-activity relationships could reveal precise molecular determinants of gating differences.

Our development of CLM142 addresses the critical need for specific M-channel therapeutics following retigabine's withdrawal (*51-54, 56, 57, 59-61, 77, 78*). This optimized compound shows major improvements over retigabine, demonstrating both 10-fold greater potency and superior specificity. Structural analysis revealed that it establishes distinct interactions with S5/S6 helices while preserving retigabine's activation mechanism. These structural innovations likely account for CLM142's improved pharmacological properties, though further optimization may yield additional clinical benefits.

Our open-state structure suggests PIP_2 mediates VSD-pore coupling through a conserved basic residue interface (R87/R117, R89/R119, R213/R242, R214/R243, K327/K366). The activation mechanism revealed by the structure is in agreement with prior studies (*44, 46-48*). While current densities were poorly resolved, future studies using PIP_2-incorporated nanodiscs or liposomes may better capture these critical interactions and reveal additional mechanistic details.

It is worth noting that our findings are subject to several limitations. First, both the structural observations and functional characterizations are based on recombinant proteins expressed in heterologous systems, which may not fully recapitulate the native neuronal environment. Second, the enhanced potency and subtype specificity of CLM142, while rigorously established under patch-clamp conditions, require further validation in

342 physiological disease models and clinical studies to substantiate its therapeutic superiority
343 over retigabine.
344
345 By elucidating the M-channel's structural principles, we have: (1) reconciled
346 conflicting stoichiometry models through demonstration of expression-dependent assembly,
347 (2) provided the first structural explanation for subthreshold activation, and (3) developed
348 CLM142 as a precision therapeutic candidate. These advances establish a framework for
349 understanding M-channel physiology and developing targeted treatments for epilepsy and
350 related disorders.
351

MATERIALS AND METHODS

Cell culture and transient transfection

Baculovirus was generated using *Sf9* insect cells cultured in Sf900-II SFM medium (GIBCO) at 28°C. Recombinant proteins were expressed in HEK293F cells maintained in SMM 293-T II serum-free medium (Sino Biological) at 37°C in a humidified incubator with 5% CO_2. Cells were infected when the density reached 2.0-3.0×10^6 cells/mL. HEK293T and CHO-K1 cells were used for electrophysiological recordings. HEK293T cells were cultured in Dulbecco's Modified Eagle Medium (DMEM; BI) supplemented with 4.5 mg/mL glucose and 10% (v/v) fetal bovine serum (FBS; BI). CHO-K1 cells were maintained in DMEM/F12 medium (Gibco) supplemented with 10% FBS and 1% (v/v) penicillin–streptomycin (Gibco). All mammalian cells were incubated at 37°C in a 5% CO_2 atmosphere. Plasmids were transfected when the cells reached ~70% confluency. HEK293T or CHO-K1 cells were transiently transfected with 2.5 μg plasmid DNA per well using Lipofectamine 3000 (Invitrogen) following the manufacturer's instructions.

Cloning, expression, and purification of M-Channel

Gene encoding human KCNQ2 (UniProt: O43526) and KCNQ3 (UniProt: O43525) were synthesized by GENEWIZ and confirmed by sequencing. KCNQ2 and KCNQ3 full-length were cloned into a pEGBacMam expression vector with an N-terminal 8×His-GFP-tag and FLAG-tag, respectively (*79*). Expression products of the two plasmids were NHis-GFP-KCNQ2 (WT) and NFlag-KCNQ3 (WT). To improve the stability and increase the production, amino acids (353-533AA) between HA and HB of the truncated KCNQ2 (64-674AA) were replaced by GS-linker (GGGSGGGS), KCNQ3 was also truncated and kept

the 93-691AA. High-resolution structures, including M-channel^{apo}, M-channel^{CLM142}, and M-channel^{open}, were obtained using plasmids engineered as described above. All plasmids were confirmed by DNA sequencing.

To express M-channel, recombinant baculoviruses was generated using Bac-to-Bac system (Thermo Fisher Scientific) as previously described (*79*). When cell density reached approximately 2.5×10^6 cells/mL, P2 viruses of KCNQ2 and KCNQ3 were co-infected into the cells at a ratio of 1:10 (v/v). After 8 h of culturing, 10 mM sodium butyrate (Sigma) was added to the medium to boost protein expression at 30 °C. Cells were harvested after ~48 hours of culturing and frozen in liquid nitrogen before being stored in a −80 °C refrigerator for future use.

For the purification of M-channel, 6L cells were solubilized in extraction buffer containing 20 mM Tris-HCl pH 8.0, 200 mM KCl, 1% DDM/CHS (10:1, w/w; Anatrace), 2 uM leupeptin, 1 uM pepstatin A, 1 ug/mL aprotinin, 1 mM PMSF for 2 hours at 4°C. Solubilized cell lysis were clarified by centrifugation at 13,000 rpm for one hour. The resulting supernatant was applied to Anti-Flag G1 Affinity Resin (GenScript) and the loaded resin was washed by wash buffer containing 20 mM Tris-HCl pH 8.0, 200 mM KCl, 1mM PMSF and 0.03% GDN (Anatrace). The protein was eluted with 200 μg/mL FLAG peptide in wash buffer and then loaded onto High Affinity Ni-Charged Resin (QIAGEN). The resin was washed by wash buffer supplemented with 30 mM imidazole and the protein was eluted with 300 mM imidazole. The eluent was concentrated by 100 kDa MWCO Amicon Ultra-4 centrifugal filter (Millipore) and then applied to size-exclusion chromatography (Superose 6 Increase, 10/300 GL, GE Healthcare) in buffer containing 20 mM Tris-HCl pH 8.0, 150 mM KCl, 1mM PMSF and 0.03% GDN. The peak fractions containing the KCNQ2/KCNQ3

complex were concentrated to about 12 mg/mL for further experiments. To prepare the sample of the M-channel with CLM142, concentrated protein was incubated with 1mM CLM142 at least 30 minutes at 4 °C prior to Cryo-EM sample preparation. To obtain the open conformation of M-channel, the purified protein was incubated with 1 mM PIP2 and 1mM CLM142. CLM142 was synthesized by the laboratory of Professor Huaiyu Yang (East China Normal University). The PIP_2 we used is 1,2-dioctanoyl-sn-glycero-3-phospho-(1'-myo-inositol-4',5'-bisphosphate) (ammonium salt) purchased from Avanti.

Cryo-EM sample preparation and data collection

To prepare Cryo-EM sample, the concentrated complex mixture (3.5 μL) was placed on glow-discharged holey carbon grids (Quantifoil Au R1.2/1.3), which were blotted for 3.5 s and flash-frozen in liquid ethane cooled by liquid nitrogen with Vitrobot (Mark IV, Thermo Fisher Scientific). The grids were loaded onto a 300 kV Titan Krios (Thermo Fisher Scientific Inc.) equipped with K3 Summit detector (Gatan) and GIF Quantum energy filter. Automated data collection was performed using EPU software (Thermo Fisher Scientific) in super-resolution mode at nominal magnification of 81,000×, with a slit width of 20 eV on the energy filter. A defocus series ranging from −1.5 μm to −2.0 μm was used. Each stack was exposed for 2.56 s with an exposure time of 0.08 s per frame, resulting in a total of 32 frames per stack and the total dose was approximately 50 e^-/Å2 for each stack. The stacks were motion corrected with MotionCor2 and binned 2 fold, resulting in a pixel size of 1.087 Å/pixel (*80*). Meanwhile, dose weighting was performed (*81*). The defocus values were estimated with Gctf (*82*).

Cryo-EM data processing

The data processing workflow for the M-channel is illustrated in figs. S5 to S7. All steps were conducted in CryoSPARC v4.6.2 (*83*). For M-channel^{WT}, a total of 5,393 micrographs were collected. Using the template picker, 5,223,566 particles were automatically selected. After particle extraction, multiple rounds of 2D classification, ab initio reconstruction, and heterogeneous refinement were performed, resulting in a dataset of 727,947 selected particles. These particles were subjected to non-uniform refinement with C1 symmetry. To distinguish between the KCNQ2 and KCNQ3 components, non-uniform refinement with C4 symmetry was performed to align the symmetry axis along the Z-axis. A new particle stack was subsequently generated via symmetry expansion using C4 symmetry. The expanded dataset was classified into two distinct VSD domain states through multiple rounds of 3D classification, using a focused mask on the VSD region. Particles corresponding to each state were grouped based on their stoichiometric ratios by intersecting different VSD classifications. The resulting particle stacks were further processed using heterogeneous refinement followed by non-uniform refinement to enhance map quality and improve resolution. A total of 16,214, 15,162, and 27,141 micrographs were collected for M-channel^{apo}, M-channel^{CLM142}, and M-channel^{open}, respectively. Two strategies were applied for the data processing. The first one followed the same procedure as described for the M-channel^{WT}. The second conducted 3D classification using four separate masks, each enclosing an individual VSD domain. Particles of identical stoichiometries were combined and refined via non-uniform refinement. CryoSieve was used to exclude unwanted particles (*84*). The resolution was estimated with the gold-standard Fourier shell correlation 0.143 criterion with high resolution noise substitution (*85, 86*).

444

445 **Model building and structure refinement**

446 The AlphaFold-predicted models of KCNQ3 (AlphaFold DB ID: O43525) and KCNQ2
447 (AlphaFold DB ID: O43526) were initially docked into the final cryo-EM density maps using
448 UCSF ChimeraX (*87-89*). Manual model building and adjustment were subsequently
449 performed in Coot v0.9.8.1, with careful attention to the chemical properties of individual
450 amino acid residues (*90*). Due to insufficient electron density, the N-terminal and C-terminal
451 regions were not modeled. Several putative lipid molecules were tentatively placed into the
452 observed densities.
453 Real-space refinement was performed using phenix.real_space_refine in PHENIX 1.20, with
454 secondary structure and geometry restraints applied throughout (*91*). To avoid overfitting,
455 gold-standard refinement was employed by alternately refining against one of the two
456 independently calculated half-maps and validating against the other. Final refinement
457 statistics and map quality metrics are summarized in Tables S1 to S5.

458

459 **Design of KCNQ2 and KCNQ3 concatemers**

460 Concatemeric constructs were created by the sequential insertion of individual subunits into
461 a pEGBacMam expression vector with an N-terminal 8×His-GFP-tag. Every subunit of
462 KCNQ2 or KCNQ3 was of wild type without deletions or truncations. Four concatemers
463 were generated: M23, M2333, M2233, and M2223. Adjacent subunits were linked by a GS-
464 linker (GGGGSSGGGGSSGGGGSS). The accuracy of the final sequence was confirmed by
465 both inserts digestion and the third-generation long-read DNA sequencing.

466

Whole-cell Electrophysiology

For the whole-cell electrophysiological experiments of the KCNQ2/KCNQ3 concatemers and chimeric constructs, the whole-cell K^+ currents were recorded in HEK293T cells using an EPC-10 amplifier with Patchmaster 2x92 software (HEKA Elektronik) and glass micropipettes (2.5-4 MΩ) made by P-1000 pipette puller (Sutter Instrument). To record the KCNQ current, the pipette solution contained 100 mM KCl, 50 mM KF, 5 mM EGTA, 10 mM HEPES, adjusted to pH 7.2 with KOH, and the bath contained 130 mM NaCl, 20 mM KCl, 1 mM $CaCl_2$, 2 mM $MgCl_2$, 5 mM D-Glucose, 10 mM HEPES, adjusted to pH 7.2 with NaOH. Fitmaster 2x92 (HEKA Elektronik) and Prism 10.1.2 (GraphPad Software) were used for data analysis.

To record the currents, a series of 2,000 ms depolarizing steps (holding potential -80 mV) was applied from -90 mV to +80 mV in 10 mV increments. Then, the cells were stimulated by -120 mV for 250 ms to obtain tail currents. The linear component of leak current and capacitive transients was subtracted using the -P/4 procedure and the voltage errors were minimized using series resistance compensation. The normalized tail current amplitude of the activation curves was plotted against step potentials and fitted by the Boltzmann Sigmoidal function:

$$\frac{I}{I_{max}} = \frac{1}{1 + \exp\left(\frac{V_{1/2} - V_m}{k}\right)}$$

Where I refers to the tail current, $V_{1/2}$ refers to the voltage for half-maximal activation, V_m refers to the test potential, and k refers to the slope of the curve.

Whole-cell K^+ currents of the M-channel/KCNQ2/KCNQ4 with CLM142/retigabine were recorded at room temperature using HEKA EPC-10 amplifier. The series resistance (Rs) was

70-80% compensated using the internal compensation program of the amplifier. The patch pipettes (World Precision Instruments) were pulled to a resistance of 3-5 MΩ. The pipette solution consisted of 140 mM KCl, 3 mM $MgCl_2$, 5 mM EGTA, 5 mM K_2ATP and 10 mM HEPES (pH 7.3, adjusted with KOH, all from Sigma-Aldrich). The extracellular solution contained 145 mM NaCl, 5 mM KCl, 1 mM $CaCl_2$, 3 mM $MgCl_2$, 10 mM D-glucose and 10 mM HEPES (pH 7.3, adjusted with NaOH).

To construct the M-channel/KCNQ2/KCNQ4 activation curves, cells were held at -80 mV and currents were elicited by a series of 2,000-ms depolarizing steps from -90 mV to +80 mV in 10-mV increments, followed by -120 mV to record tail currents. Activation curves were fitted by the Boltzmann equation: $I_{tail} = (I_{max} - I_{min})/[1 + \exp(V_{1/2} - V_m)/k] + I_{min}$, where I_{tail} is the normalized tail current recorded immediately after stepping to -120 mV from different preceding V_m levels, I_{max} and I_{min} are the maximum and minimum normalized tail currents, respectively, $V_{1/2}$ is the half-maximal activation voltage, and k is the slope factor of the curve. Also, this protocol was used to study the M-channel channel activation kinetics. The M-channel deactivation kinetics were measured by tail currents elicited by a hyperpolarizing voltage of -120 mV for 1,200 ms after a 2,000-ms depolarized potential of +50 mV, with a holding potential of -80 mV. The activation and deactivation traces were fitted to a single exponential function: $I = A \times [1 - \exp(-t/tau)] + I_0$, where I is the current, I_0 is the steady-state amplitude of the current, A is the difference between the peak and steady-state current amplitudes; t is time; and tau is the time constant. The concentration–response curves were analyzed by three parameters logistics regression model. For recordings of KCNQ4 channel currents, pipettes were filled with the intracellular solution of the following composition: 150 mM KCl, 3 mM $MgCl_2$, 5 mM EGTA and 10 mM HEPES (pH 7.3, adjusted

with KOH). Extracellular solution contained 145 mM NaCl, 5 mM KCl, 1 mM $CaCl_2$, 3 mM $MgCl_2$ and 10 mM HEPES (pH 7.4, adjusted with NaOH). The methods used to record KCNQ4 were the same as those used to record M-channel currents.

Processed by Clampfit 10.4, patch clamp data were analyzed in GraphPad Prism 8.0.2. An unpaired two-tailed Student's *t*-test was used to determine significance between groups. n.s. indicates no significance. *$p < 0.05$, **$p < 0.01$, ***$p < 0.001$, and ****$p < 0.0001$. All data are presented as mean ± SEM.

Inside-out single-channel recordings

Inside-out recordings were performed 48 hours after transfection using EPC10-USB amplifier (HEKA). Patch recordings were digitized at 10 kHz and filtered at 2 kHz. The bath solution contained 175 mM KCl, 4 mM $MgCl_2$, and 10 mM HEPES (pH 7.4, adjusted with KOH). The pipette solution was 150 mM NaCl, 5 mM KCl, 1 mM $MgCl_2$, and 10 mM HEPES (pH 7.4, adjusted with NaOH). The patch pipette was pulled to a resistance of 8–12 MΩ. Single-channel statistical analysis was conducted by Clampfit 10.4 software. All-point histograms were fitted with Gaussian functions to obtain the mean single-channel current (i). Single-channel conductance (γ) was obtained by the equation $\gamma = i/(V - V_E)$, where V is the test potential and V_E is the reversal potential of potassium.

Synthetic scheme of CLM142

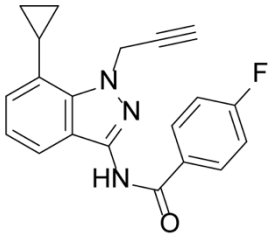

CLM142 (**1**)

Synthetic Route:

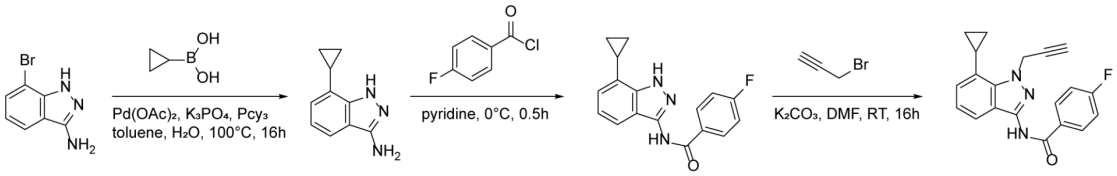

Step 1: 7-cyclopropyl-1H-indazol-3-amine

7-bromo-1H-indazol-3-amine (**2**, 2.00 g, 9.43 mmol) was dissolved in toluene (20 mL) and water (6 mL). Cyclopropylboronic acid (5.67 g, 66.01 mmol), tricyclohexylphosphine (0.53 g, 1.89 mmol), potassium phosphate (6.01 g, 28.29 mmol) and palladium acetate (0.42 g, 1.89 mmol) were added sequentially. Under nitrogen protection, the mixture was heated to 100 °C and stirred for 16 hours. TLC (PE:EA = 1:1, Rf = 0.1) indicated the complete consumption of the starting material. The reaction solution was cooled to room temperature, filtered through Celite, quenched with water (10 mL), and extracted with ethyl acetate (10 mL × 3). The combined organic phases were washed with saturated brine (20 mL × 3), dried over anhydrous sodium sulfate, and concentrated. The crude product was purified by silica gel column chromatography (PE:EA = 2:1 - 2:3) to afford the title compound **3** as a white solid (0.69 g, yield 42%).

LC-MS: m/z = 174.2 $[M+H]^+$

549 Step 2: N-(7-cyclopropyl-1H-indazol-3-yl)-4-fluorobenzamide

550 Compound **3** (380 mg, 2.19 mmol) was dissolved in pyridine (2 mL), cooled to 0 °C, and 4-
551 fluorobenzoyl chloride (347 mg, 2.19 mmol) was added dropwise. The mixture was stirred
552 at this temperature for 30 minutes. TLC (PE:EA = 1:1, Rf = 0.4) showed the complete
553 reaction of the starting material. The reaction was quenched with water (10 mL) and
554 extracted with ethyl acetate (10 mL × 3). The combined organic phases were washed with
555 saturated brine (20 mL × 3), dried over anhydrous sodium sulfate, and concentrated. The
556 crude product was purified by silica gel column chromatography (PE:EA = 5:1 - 2:1) to
557 obtain the title Compound **4** as a brown solid (325 mg, yield 50%).

558 LC-MS: m/z = 296.1 $[M+H]^+$

559 Step 3: N-(7-cyclopropyl-1-(prop-2-yn-1-yl)-1H-indazol-3-yl)-4-fluorobenzamide

560 Compound **4** (80 mg, 0.27 mmol) was dissolved in N,N-dimethylformamide (2 mL). 3-
561 bromopropyne (39 mg, 0.33 mmol) and potassium carbonate (75 mg, 0.54 mmol) were
562 added at room temperature, and the mixture was stirred at room temperature for 16 hours.
563 TLC (PE:EA = 2:1, Rf = 0.4) indicated a small amount of starting material remaining. The
564 reaction was quenched with water (10 mL) and extracted with ethyl acetate (10 mL × 3).
565 The combined organic phases were washed with saturated brine (20 mL × 3), dried over
566 anhydrous sodium sulfate, and concentrated. Purification by preparative HPLC (TFA) gave
567 the title compound CLM142 (**1**) as a white solid (18 mg, yield 20%).

568 LC-MS: m/z = 334.2 $[M+H]^+$

569 HPLC:99.10% purity, 220 nm

570 ^{1}HNMR (400 MHz, *DMSO-d6*) δ 10.88 (s, 1H), 8.15 (dd, J = 8.4, 5.6 Hz, 2H), 7.53 (d, J =

571 8.4 Hz, 1H), 7.39 (t, J = 8.8 Hz, 2H), 7.17 (d, J = 7.2 Hz, 1H), 7.04 (t, J = 8.0 Hz, 1H), 5.56

572 (d, J = 1.6 Hz, 2H), 3.44 (s, 1H), 2.49-2.44 (m, 1H), 1.10-1.05 (m, 2H), 0.89-0.83 (m, 2H).

573

REFERENCES AND NOTES

1. W.-P. Yang *et al.*, Functional expression of two KvLQT1-related potassium channels responsible for an inherited idiopathic epilepsy. *Journal of Biological Chemistry* **273**, 19419-19423 (1998).
2. H. S. Wang *et al.*, KCNQ2 and KCNQ3 potassium channel subunits: molecular correlates of the M-channel. *Science* **282**, 1890-1893 (1998).
3. B. C. Schroeder, C. Kubisch, V. Stein, T. J. Jentsch, Moderate loss of function of cyclic-AMP-modulated KCNQ2/KCNQ3 K+ channels causes epilepsy. *Nature* **396**, 687-690 (1998).
4. D. A. Brown, P. R. Adams, Muscarinic suppression of a novel voltage-sensitive K+ current in a vertebrate neurone. *Nature* **283**, 673-676 (1980).
5. T. J. Jentsch, Neuronal KCNQ potassium channels: physislogy and role in disease. *Nat Rev Neurosci* **1**, 21-30 (2000).
6. S. Maljevic, T. V. Wuttke, H. Lerche, Nervous system KV7 disorders: breakdown of a subthreshold brake. *J Physiol* **586**, 1791-1801 (2008).
7. N. V. Marrion, Control of M-current. *Annu Rev Physiol* **59**, 483-504 (1997).
8. P. Delmas, D. A. Brown, Pathways modulating neural KCNQ/M (Kv7) potassium channels. *Nat Rev Neurosci* **6**, 850-862 (2005).
9. D. L. Greene, N. Hoshi, Modulation of Kv7 channels and excitability in the brain. *Cell Mol Life Sci* **74**, 495-508 (2017).
10. B. P. Bean, The action potential in mammalian central neurons. *Nat Rev Neurosci* **8**, 451-465 (2007).
11. C. Yue, Y. Yaari, KCNQ/M channels control spike afterdepolarization and burst generation in hippocampal neurons. *J Neurosci* **24**, 4614-4624 (2004).
12. E. C. Cooper *et al.*, Colocalization and coassembly of two human brain M-type potassium channel subunits that are mutated in epilepsy. *Proceedings of the National Academy of Sciences* **97**, 4914-4919 (2000).
13. N. A. Singh *et al.*, A novel potassium channel gene, KCNQ2, is mutated in an inherited epilepsy of newborns. *Nat Genet* **18**, 25-29 (1998).
14. C. Biervert *et al.*, A potassium channel mutation in neonatal human epilepsy. *Science* **279**, 403-406 (1998).
15. C. Charlier *et al.*, A pore mutation in a novel KQT-like potassium channel gene in an idiopathic epilepsy family. *Nat Genet* **18**, 53-55 (1998).
16. N. Tinel, I. Lauritzen, C. Chouabe, M. Lazdunski, M. Borsotto, The KCNQ2 potassium channel: splice variants, functional and developmental expression. Brain localization and comparison with KCNQ3. *FEBS Lett* **438**, 171-176 (1998).
17. M. Schwake, M. Pusch, T. Kharkovets, T. J. Jentsch, Surface expression and single channel properties of KCNQ2/KCNQ3, M-type K+ channels involved in epilepsy. *J Biol Chem* **275**, 13343-13348 (2000).
18. W. P. Yang *et al.*, Functional expression of two KvLQT1-related potassium channels responsible for an inherited idiopathic epilepsy. *J Biol Chem* **273**, 19419-19423 (1998).
19. B. E. Grinton *et al.*, Familial neonatal seizures in 36 families: Clinical and genetic features correlate with outcome. *Epilepsia* **56**, 1071-1080 (2015).

20. F. Zara *et al.*, Genetic testing in benign familial epilepsies of the first year of life: clinical and diagnostic significance. *Epilepsia* **54**, 425-436 (2013).
21. K. Dedek *et al.*, Myokymia and neonatal epilepsy caused by a mutation in the voltage sensor of the KCNQ2 K+ channel. *Proc Natl Acad Sci U S A* **98**, 12272-12277 (2001).
22. N. A. Singh *et al.*, KCNQ2 and KCNQ3 potassium channel genes in benign familial neonatal convulsions: expansion of the functional and mutation spectrum. *Brain* **126**, 2726-2737 (2003).
23. N. Trump *et al.*, Improving diagnosis and broadening the phenotypes in early-onset seizure and severe developmental delay disorders through gene panel analysis. *J Med Genet* **53**, 310-317 (2016).
24. E. Miraglia del Giudice *et al.*, Benign familial neonatal convulsions (BFNC) resulting from mutation of the KCNQ2 voltage sensor. *Eur J Hum Genet* **8**, 994-997 (2000).
25. T. S. Surti, L. Huang, Y. N. Jan, L. Y. Jan, E. C. Cooper, Identification by mass spectrometry and functional characterization of two phosphorylation sites of KCNQ2/KCNQ3 channels. *Proc Natl Acad Sci U S A* **102**, 17828-17833 (2005).
26. S. Hirose *et al.*, A novel mutation of KCNQ3 (c.925T-->C) in a Japanese family with benign familial neonatal convulsions. *Ann Neurol* **47**, 822-826 (2000).
27. C. Biervert *et al.*, A potassium channel mutation in neonatal human epilepsy. *Science* **279**, 403-406 (1998).
28. F. Miceli, M. V. Soldovieri, S. Weckhuysen, E. Cooper, M. Taglialatela, KCNQ2-related disorders. (2022).
29. S. Weckhuysen *et al.*, KCNQ2 encephalopathy: emerging phenotype of a neonatal epileptic encephalopathy. *Annals of neurology* **71**, 15-25 (2012).
30. S. Dimassi *et al.*, Whole-exome sequencing improves the diagnosis yield in sporadic infantile spasm syndrome. *Clin Genet* **89**, 198-204 (2016).
31. R. Borgatti *et al.*, A novel mutation in KCNQ2 associated with BFNC, drug resistant epilepsy, and mental retardation. *Neurology* **63**, 57-65 (2004).
32. M. Kato *et al.*, Clinical spectrum of early onset epileptic encephalopathies caused by KCNQ2 mutation. *Epilepsia* **54**, 1282-1287 (2013).
33. S. Syrbe *et al.*, De novo loss-or gain-of-function mutations in KCNA2 cause epileptic encephalopathy. *Nat Genet* **47**, 393-399 (2015).
34. A. Nissenkorn *et al.*, Donepezil as a new therapeutic potential in KCNQ2-and KCNQ3-related autism. *Front Cell Neurosci* **18**, 1380442 (2024).
35. M. Siracusano, C. Marcovecchio, A. Riccioni, C. Dante, L. Mazzone, Autism spectrum disorder and a De Novo Kcnq2 gene mutation: a case report. *Pediatric Reports* **14**, 200-206 (2022).
36. K. Springer, N. Varghese, A. V. Tzingounis, Flexible Stoichiometry: Implications for KCNQ2- and KCNQ3-Associated Neurodevelopmental Disorders. *Dev Neurosci* **43**, 191-200 (2021).
37. T. T. Sands *et al.*, Autism and developmental disability caused by KCNQ3 gain-of-function variants. *Annals of neurology* **86**, 181-192 (2019).
38. T. S. Surti, L. Y. Jan, A potassium channel, the M-channel, as a therapeutic target. *Curr Opin Investig Drugs* **6**, 704-711 (2005).

39. X. Li *et al.*, Molecular basis for ligand activation of the human KCNQ2 channel. *Cell Res* **31**, 52-61 (2021).
40. J. K. Hadley *et al.*, Stoichiometry of expressed KCNQ2/KCNQ3 potassium channels and subunit composition of native ganglionic M channels deduced from block by tetraethylammonium. *J Neurosci* **23**, 5012-5019 (2003).
41. A. P. Stewart *et al.*, The Kv7.2/Kv7.3 heterotetramer assembles with a random subunit arrangement. *J Biol Chem* **287**, 11870-11877 (2012).
42. M. S. Shapiro *et al.*, Reconstitution of muscarinic modulation of the KCNQ2/KCNQ3 K(+) channels that underlie the neuronal M current. *J Neurosci* **20**, 1710-1721 (2000).
43. J. Sun, R. MacKinnon, Cryo-EM Structure of a KCNQ1/CaM Complex Reveals Insights into Congenital Long QT Syndrome. *Cell* **169**, 1042-1050 e1049 (2017).
44. J. Sun, R. MacKinnon, Structural Basis of Human KCNQ1 Modulation and Gating. *Cell* **180**, 340-347 e349 (2020).
45. T. Li *et al.*, Structural Basis for the Modulation of Human KCNQ4 by Small-Molecule Drugs. *Mol Cell* **81**, 25-37 e24 (2021).
46. Y. Zheng *et al.*, Structural insights into the lipid and ligand regulation of a human neuronal KCNQ channel. *Neuron* **110**, 237-247 e234 (2022).
47. Z. Yang *et al.*, Phosphatidylinositol 4,5-bisphosphate activation mechanism of human KCNQ5. *Proc Natl Acad Sci U S A* **122**, e2416738122 (2025).
48. S. Zhang *et al.*, A small-molecule activation mechanism that directly opens the KCNQ2 channel. *Nature Chemical Biology* **20**, 847-856 (2024).
49. N. D. Yang *et al.*, Electro-mechanical coupling of KCNQ channels is a target of epilepsy-associated mutations and retigabine. *Sci Adv* **8**, eabo3625 (2022).
50. V. Telezhkin, D. A. Brown, A. J. Gibb, Distinct subunit contributions to the activation of M-type potassium channels by PI(4,5)P2. *J Gen Physiol* **140**, 41-53 (2012).
51. Y. Liu, X. Bian, K. Wang, Pharmacological Activation of Neuronal Voltage-Gated Kv7/KCNQ/M-Channels for Potential Therapy of Epilepsy and Pain. *Handb Exp Pharmacol* **267**, 231-251 (2021).
52. V. Barrese, J. B. Stott, I. A. Greenwood, KCNQ-Encoded Potassium Channels as Therapeutic Targets. *Annu Rev Pharmacol Toxicol* **58**, 625-648 (2018).
53. M. J. Gunthorpe, C. H. Large, R. Sankar, The mechanism of action of retigabine (ezogabine), a first-in-class K+ channel opener for the treatment of epilepsy. *Epilepsia* **53**, 412-424 (2012).
54. L. Tatulian, P. Delmas, F. C. Abogadie, D. A. Brown, Activation of expressed KCNQ potassium currents and native neuronal M-type potassium currents by the anti-convulsant drug retigabine. *J Neurosci* **21**, 5535-5545 (2001).
55. J. E. Linley, L. Pettinger, D. Huang, N. Gamper, M channel enhancers and physiological M channel block. *J Physiol* **590**, 793-807 (2012).
56. R. J. Porter, V. Nohria, C. Rundfeldt, Retigabine. *Neurotherapeutics* **4**, 149-154 (2007).
57. J. A. French *et al.*, Randomized, double-blind, placebo-controlled trial of ezogabine (retigabine) in partial epilepsy. *Neurology* **76**, 1555-1563 (2011).
58. C. Rundfeldt, The new anticonvulsant retigabine (D-23129) acts as an opener of K+ channels in neuronal cells. *Eur J Pharmacol* **336**, 243-249 (1997).

59. N. Brickel, P. Gandhi, K. VanLandingham, J. Hammond, S. DeRossett, The urinary safety profile and secondary renal effects of retigabine (ezogabine): a first-in-class antiepileptic drug that targets KCNQ (K(v)7) potassium channels. *Epilepsia* **53**, 606-612 (2012).
60. J. Daniluk, J. A. Cooper, M. Stender, A. Kowalczyk, Survey of Physicians' Understanding of Specific Risks Associated with Retigabine. *Drugs Real World Outcomes* **3**, 155-163 (2016).
61. M. A. Faulkner, R. A. Burke, Safety profile of two novel antiepileptic agents approved for the treatment of refractory partial seizures: ezogabine (retigabine) and perampanel. *Expert Opin Drug Saf* **12**, 847-855 (2013).
62. Y. Jiang *et al.*, X-ray structure of a voltage-dependent K+ channel. *Nature* **423**, 33-41 (2003).
63. M. Schwake, M. Pusch, T. Kharkovets, T. J. Jentsch, Surface expression and single channel properties of KCNQ2/KCNQ3, M-type K+ channels involved in epilepsy. *Journal of Biological Chemistry* **275**, 13343-13348 (2000).
64. X. Tao, A. Lee, W. Limapichat, D. A. Dougherty, R. MacKinnon, A gating charge transfer center in voltage sensors. *Science* **328**, 67-73 (2010).
65. X. Zhang, N. Yan, The conformational shifts of the voltage sensing domains between Na(v)Rh and Na(v)Ab. *Cell Res* **23**, 444-447 (2013).
66. M. A. Zaydman, J. Cui, PIP2 regulation of KCNQ channels: biophysical and molecular mechanisms for lipid modulation of voltage-dependent gating. *Front Physiol* **5**, 195 (2014).
67. Y. Li, N. Gamper, D. W. Hilgemann, M. S. Shapiro, Regulation of Kv7 (KCNQ) K+ channel open probability by phosphatidylinositol 4,5-bisphosphate. *J Neurosci* **25**, 9825-9835 (2005).
68. M. A. Zaydman *et al.*, Kv7.1 ion channels require a lipid to couple voltage sensing to pore opening. *Proc Natl Acad Sci U S A* **110**, 13180-13185 (2013).
69. P. Delmas, D. A. Brown, Pathways modulating neural KCNQ/M (Kv7) potassium channels. *Nat Rev Neurosci* **6**, 850-862 (2005).
70. J. Li *et al.*, Small molecule inhibits KCNQ channels with a non-blocking mechanism. *Nature Chemical Biology*, 1-10 (2025).
71. N. Dirkx, F. Miceli, M. Taglialatela, S. Weckhuysen, The role of Kv7. 2 in neurodevelopment: insights and gaps in our understanding. *Frontiers in Physiology* **11**, 570588 (2020).
72. J. K. Hadley *et al.*, Stoichiometry of expressed KCNQ2/KCNQ3 potassium channels and subunit composition of native ganglionic M channels deduced from block by tetraethylammonium. *Journal of Neuroscience* **23**, 5012-5019 (2003).
73. T. Kanaumi *et al.*, Developmental changes in KCNQ2 and KCNQ3 expression in human brain: possible contribution to the age-dependent etiology of benign familial neonatal convulsions. *Brain and Development* **30**, 362-369 (2008).
74. F. Klinger, G. Gould, S. Boehm, M. S. Shapiro, Distribution of M-channel subunits KCNQ2 and KCNQ3 in rat hippocampus. *Neuroimage* **58**, 761-769 (2011).
75. T. Kanaumi *et al.*, Developmental changes in KCNQ2 and KCNQ3 expression in human brain: possible contribution to the age-dependent etiology of benign familial neonatal convulsions. *Brain Dev* **30**, 362-369 (2008).

76. J. D. Osteen *et al.*, Allosteric gating mechanism underlies the flexible gating of KCNQ1 potassium channels. *Proc Natl Acad Sci U S A* **109**, 7103-7108 (2012).
77. A. Zahra, R. Liu, J. Wang, J. Wu, Identifying the mechanism of action of the Kv7 channel opener, retigabine in the treatment of epilepsy. *Neurol Sci* **44**, 3819-3825 (2023).
78. G. Orhan, T. V. Wuttke, A. T. Nies, M. Schwab, H. Lerche, Retigabine/Ezogabine, a KCNQ/K(V)7 channel opener: pharmacological and clinical data. *Expert Opin Pharmacother* **13**, 1807-1816 (2012).
79. A. Goehring *et al.*, Screening and large-scale expression of membrane proteins in mammalian cells for structural studies. *Nat Protoc* **9**, 2574-2585 (2014).
80. S. Q. Zheng *et al.*, MotionCor2: anisotropic correction of beam-induced motion for improved cryo-electron microscopy. *Nat Methods* **14**, 331-332 (2017).
81. T. Grant, N. Grigorieff, Measuring the optimal exposure for single particle cryo-EM using a 2.6 A reconstruction of rotavirus VP6. *Elife* **4**, e06980 (2015).
82. K. Zhang, Gctf: Real-time CTF determination and correction. *J Struct Biol* **193**, 1-12 (2016).
83. A. Punjani, J. L. Rubinstein, D. J. Fleet, M. A. Brubaker, cryoSPARC: algorithms for rapid unsupervised cryo-EM structure determination. *Nat Methods* **14**, 290-296 (2017).
84. J. Zhu *et al.*, A minority of final stacks yields superior amplitude in single-particle cryo-EM. *Nat. Commun.* **14**, 7822 (2023).
85. P. B. Rosenthal, R. Henderson, Optimal determination of particle orientation, absolute hand, and contrast loss in single-particle electron cryomicroscopy. *J Mol Biol* **333**, 721-745 (2003).
86. S. Chen *et al.*, High-resolution noise substitution to measure overfitting and validate resolution in 3D structure determination by single particle electron cryomicroscopy. *Ultramicroscopy* **135**, 24-35 (2013).
87. M. Varadi *et al.*, AlphaFold Protein Structure Database in 2024: providing structure coverage for over 214 million protein sequences. *Nucleic Acids Res* **52**, D368-D375 (2024).
88. J. Jumper *et al.*, Highly accurate protein structure prediction with AlphaFold. *Nature* **596**, 583-589 (2021).
89. E. F. Pettersen *et al.*, UCSF ChimeraX: Structure visualization for researchers, educators, and developers. *Protein Sci* **30**, 70-82 (2021).
90. P. Emsley, B. Lohkamp, W. G. Scott, K. Cowtan, Features and development of Coot. *Acta Crystallogr D Biol Crystallogr* **66**, 486-501 (2010).
91. P. D. Adams *et al.*, PHENIX: a comprehensive Python-based system for macromolecular structure solution. *Acta Crystallogr D Biol Crystallogr* **66**, 213-221 (2010).
92. E. F. Pettersen *et al.*, UCSF ChimeraX: Structure visualization for researchers, educators, and developers. *Protein science* **30**, 70-82 (2021).
93. F. Madeira *et al.*, The EMBL-EBI Job Dispatcher sequence analysis tools framework in 2024. *Nucleic acids research* **52**, W521-W525 (2024).
94. X. Robert, P. Gouet, Deciphering key features in protein structures with the new ENDscript server. *Nucleic acids research* **42**, W320-W324 (2014).

Acknowledgments

We thank the Cryo-EM Facility and the HPC Center of Westlake University for providing data collection and computation support, respectively. We are also thankful for the support of the East China Normal University Multifunctional Platform for Innovation (001).

Funding: This work was supported by grants from the National Key Research and Development Program of China (2024YFA0916903 to H.S. and 2022YFE0205600 to H.Y.), the National Natural Science Foundation of China (82373792 to H.Y.), the Zhejiang Provincial Natural Science Foundation (DQ24C050001 to H.S.), the Research Center for Industries of the Future (RCIF), Westlake University, the Westlake Education Foundation (to H.S.), and the East China Normal University Medicine and Health Joint Fund (2022JKXYD07001 to H.Y.). **Author contributions**: The project was conceived by H.S. Y.W. and Hui Yang performed molecular cloning, protein purification, sample preparation, and cryo-EM micrograph collection. Y.Q. carried out cryo-EM data processing, structure determination, and model building. J.L. identified the CLM142 activator and conducted electrophysiological studies under the supervision of Huaiyu Yang. Y.Y. synthesized the CLM142 molecule. W.H. performed electrophysiological characterization of KCNQ2 and KCNQ3 concatemers and chimeras under the supervision of K.W. G.X. validated the sequences of KCNQ2 and KCNQ3 concatemers using third-generation sequencing data under the supervision of X.W. All authors contributed to data analysis. H.S. and Huaiyu Yang wrote the manuscript with intellectual input from all authors. **Competing interests**: J. Li and H.Y. are inventors of patent application 202311463618.7 that covers the potential usage of CLM142. The authors declare no other competing interests. **Data and materials availability**: Atomic coordinates and EM maps of

M-channels reported in this study ($M2223^{WT}$: XXXX and EMD-XXXXX; $M2223^{apo}$: XXXX and EMD-XXXXX; $M2223^{CLM142}$: XXXX and EMD-XXXXX; $M2223^{open}$: XXXX and EMD-XXXXX) have been deposited in the Protein Data Bank (http://www.rcsb.org) and the Electron Microscopy Data Bank (https://www.ebi.ac.uk/pdbe/emdb/).

Supplementary Materials

Figs. S1-S17

Tables S1-S5

References and notes

Figure legends

Fig. 1 | Structural architecture and stoichiometric flexibility of the human M-channel. (**A**) Cryo-EM reconstructions of the four distinct M-channel stoichiometries (M2223, M2233, M2323, M2333) with their relative abundances indicated. KCNQ2 and KCNQ3 subunits are colored blue and yellow, respectively. (**B**) Representative cryo-EM density map for the M2223^{apo} configuration. (**C**) Atomic model corresponding to the map in (B), displayed in three orthogonal views. (**D**) Differential positioning of the voltage-sensing domains (VSDs) relative to the pore domain (PD) in KCNQ2 versus KCNQ3, illustrated by a comparison of their tilt angles. (**E**) Structural alignment of M2223^{apo} and KCNQ2 homotetramer highlighting the differential positioning of their VSDs. (**F**) The extracellular loop (ECL) of KCNQ3 is markedly longer than that of KCNQ2, resulting in a pronounced difference in cryo-EM density. (**G**) High-resolution features that enable unambiguous subunit discrimination, including characteristic side chain densities for Y284, Y226, and F316 in KCNQ2 and T323, C255, and L355 in KCNQ3 within the pore domain. All structure figures are generated in ChimeraX (*92*).

Fig. 2 | Concatemeric KCNQ2/KCNQ3 channels recapitulate wild-type M-channel properties. (**A**) Left: Whole-cell recording protocol. Right: Representative current traces from wild-type M-channels (KCNQ2/KCNQ3 co-expression). Currents were elicited by 2 s depolarizing steps from –90 to +80 mV in 10 mV increments from a holding potential of –80 mV, followed by a –120 mV tail pulse (250 ms). (**B**) Schematic representations of the engineered concatemeric constructs with defined KCNQ2 (blue) and KCNQ3 (yellow) subunit stoichiometries. (**C**) Whole-cell current-

voltage (I-V) relationships for the indicated concatemers and wild-type channels. (**D**) Half-maximal activation voltages ($V_{1/2}$) show that all concatemeric channels exhibit significantly hyperpolarized activation compared to KCNQ2 homomers, recapitulating the wild-type M-channel phenotype. (**E**) Representative single-channel current traces for each concatemeric variant. Scale bars: 1.5 pA (vertical), 500 ms (horizontal). (**F**) Summary of unitary current amplitudes from single-channel recordings. (**G**) Summary of open probability (Po) for each concatemeric channel. Data in (**C**), (**D**), (**F**), and (**G**) are presented as mean ± SEM ($n \geq 10$). Statistical significance was determined by an unpaired two-tailed Student's *t*-test (*$p < 0.05$, **$p < 0.01$, ***$p < 0.001$, ****$p < 0.0001$).

Fig. 3 | The KCNQ3 voltage-sensing domain confers hyperpolarized activation kinetics. (**A**) Structural comparison of the voltage-sensing domains (VSDs) from KCNQ2 (blue) and KCNQ3 (yellow) in the M2223^{apo} structure. The relative positions of the S4 arginine residues (R2–R6) to the charge transfer center (CTC) on S2 reveal that the KCNQ3 VSD adopts a more depolarized conformation. (**B**) Design strategy for chimeric constructs in which the VSDs were swapped between KCNQ2 and KCNQ3, creating VSD_3-PD_2 and VSD_2-PD_3 subunits. (**C**) Whole-cell current-voltage (I-V) relationships for wild-type and chimeric channels. (**D**) Half-maximal activation voltages ($V_{1/2}$) show that channels incorporating the KCNQ3 VSD (VSD_3-PD_2 + KCNQ3) activate at more hyperpolarized potentials, while channels with the KCNQ2 VSD (VSD_2-PD_3 + KCNQ2) exhibit depolarized activation akin to KCNQ2

878 homomers. Data are presented as mean ± SEM (n ≥ 12). Statistical significance was
879 determined by an unpaired two-tailed Student's *t*-test (****p < 0.0001).
880
881 **Fig. 4 | CLM142 is a potent and selective M-channel activator with superior properties**
882 **to retigabine.** (**A**) Chemical structure of the novel M-channel activator CLM142, with key
883 functional groups labeled. (**B**) Chemical structure of the canonical M-channel activator
884 retigabine for comparison. (**C**) Representative whole-cell current traces from M-channel
885 showing potent activation by 1 μM CLM142. (**D**) Left: Concentration-dependent
886 conductance-voltage (G-V) relationships for CLM142. Right: Summary of the
887 concentration-dependent hyperpolarizing shifts in the half-maximal activation voltage
888 ($\Delta V_{1/2}$) induced by CLM142. (**E**) Left: Concentration-dependent G-V relationships for
889 retigabine. Right: Summary of the $\Delta V_{1/2}$ shifts induced by retigabine. CLM142 exhibits an
890 approximate 10-fold greater potency (EC_{50} = 0.19 ± 0.09 μM) than retigabine (EC_{50} = 2.16
891 ± 0.15 μM). (**F**) G-V curves showing the weak effect of CLM142 on homomeric KCNQ4
892 channels. (**G**) Quantitative comparison of the $\Delta V_{1/2}$ induced by CLM142 on human M-
893 channel versus KCNQ4, demonstrating CLM142's high selectivity for the neuronal M-
894 channel. Data in (**D-G**) are presented as mean ± SEM (n ≥ 5).
895
896 **Fig. 5 | Structural basis for potent activation of the M-channel by CLM142.** (**A**) Cryo-
897 EM density map of the $M2223^{CLM142}$ complex. (**B**) Atomic model of the
898 $M2223^{CLM142}$ complex, displayed in two orthogonal views. (**C**) Detailed architecture of the
899 CLM142 binding pocket, located at the interface between the S5 and S6 helices of adjacent
900 subunits. Four drug molecules (black) are present per tetramer. CLM142 forms extensive

hydrophobic and π-π stacking interactions with surrounding residues, with the atomic model showing excellent agreement with the high-resolution cryo-EM density. (**D**) Activation mechanism. Binding of CLM142 induces a displacement of the conserved tryptophan (W236 in KCNQ2; W265 in KCNQ3) and a clockwise rotation of the S5 helices (intracellular view), which favors the activation of the pore domain.

Fig. 6 | Structural elucidation of the PIP_2-dependent M-channel open state. (**A**) Cryo-EM density map of the PIP_2-bound $M2223^{open}$ structure. (**B**) Atomic model of the activated, PIP_2-bound $M2223^{open}$ structure, displayed in two orthogonal views. (**C**) Structural visualization of the pore radius in the closed ($M2223^{CLM142}$, left) and open ($M2223^{open}$, right) states. Key constriction residues are labeled. (**D**) Quantitative analysis of the pore radius along the ion permeation pathway for the closed (blue) and open (red) states, confirming gate opening. (**E**) Conformational changes in the S6 helices during channel activation, highlighting the rearrangement that underlies pore dilation. (**F**) The PIP_2 binding site at the interface of the voltage-sensing domain (VSD), S4-S5 linker, and S6 helix. The negatively charged PIP_2 headgroup is coordinated by a constellation of basic residues (R87/R117, R89/R119, R213/R242, R214/R243, K327/K366; KCNQ2/KCNQ3 numbering).

Figure 1

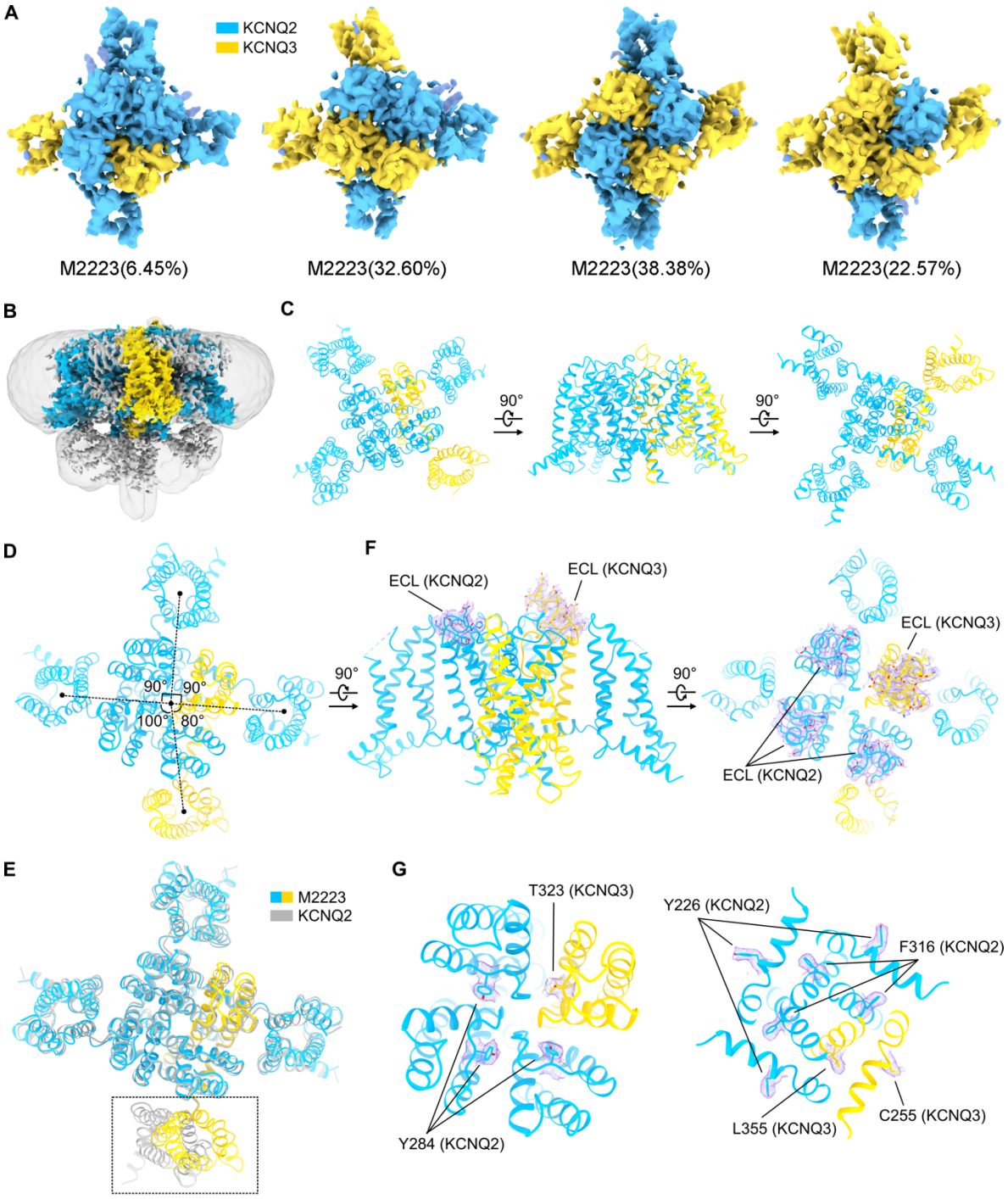

Figure 2

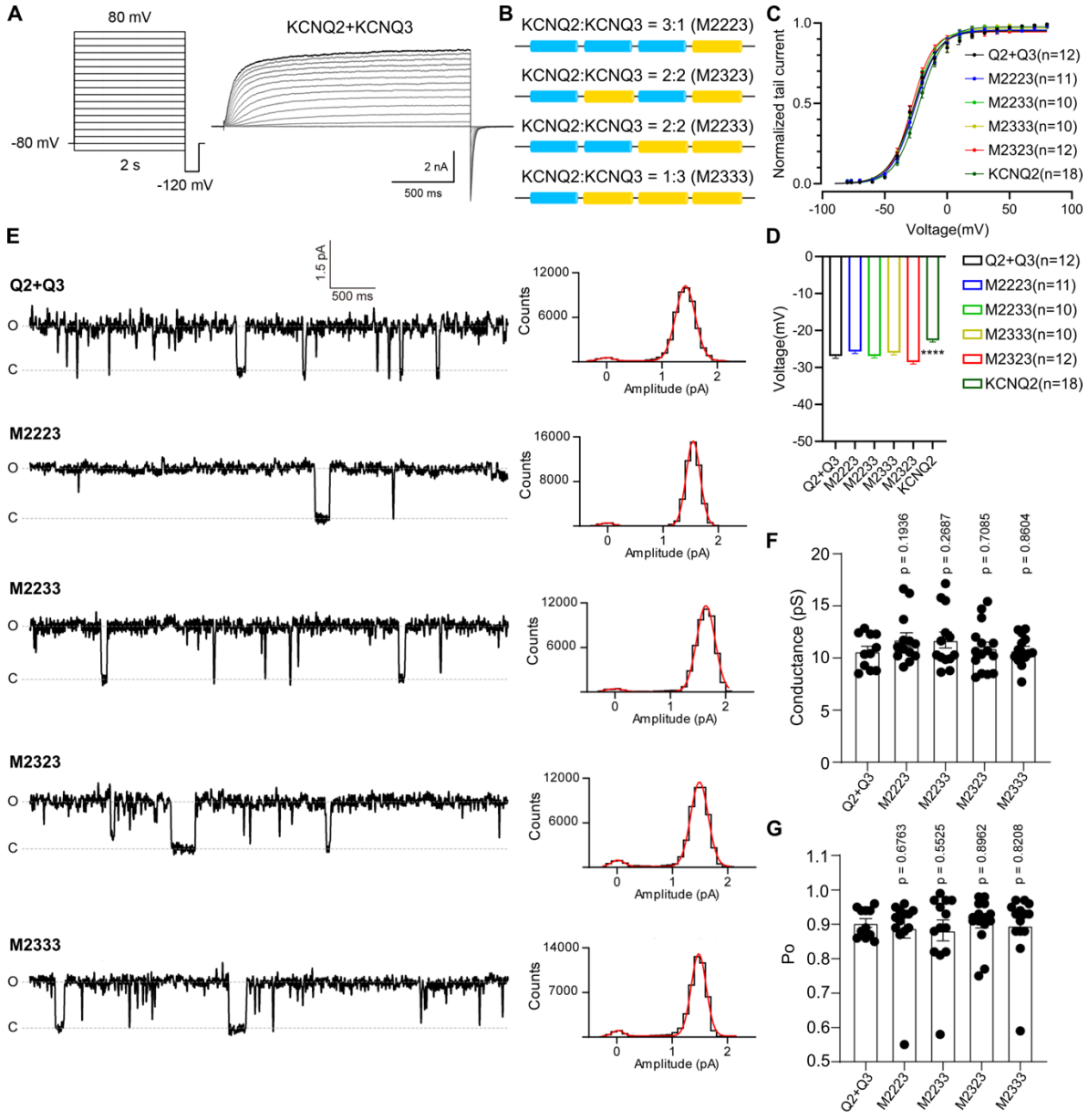

926 **Figure 3**

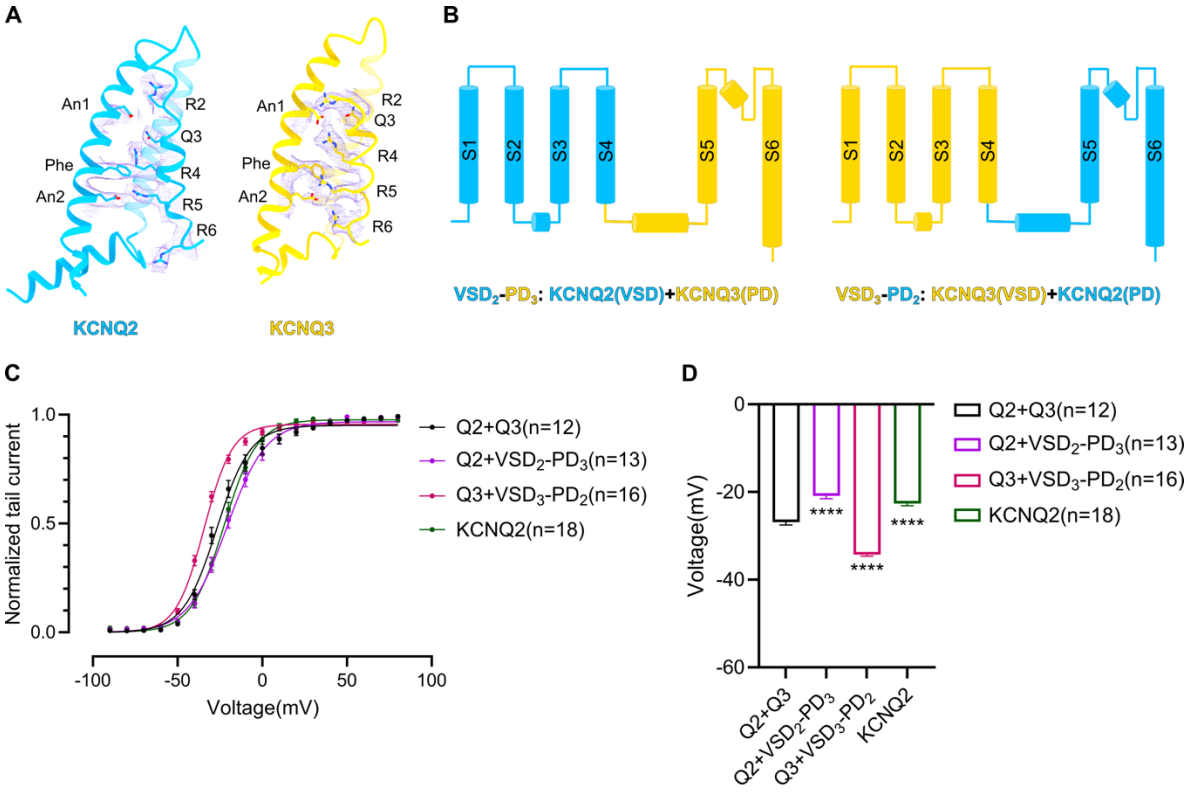

927

928

Figure 4

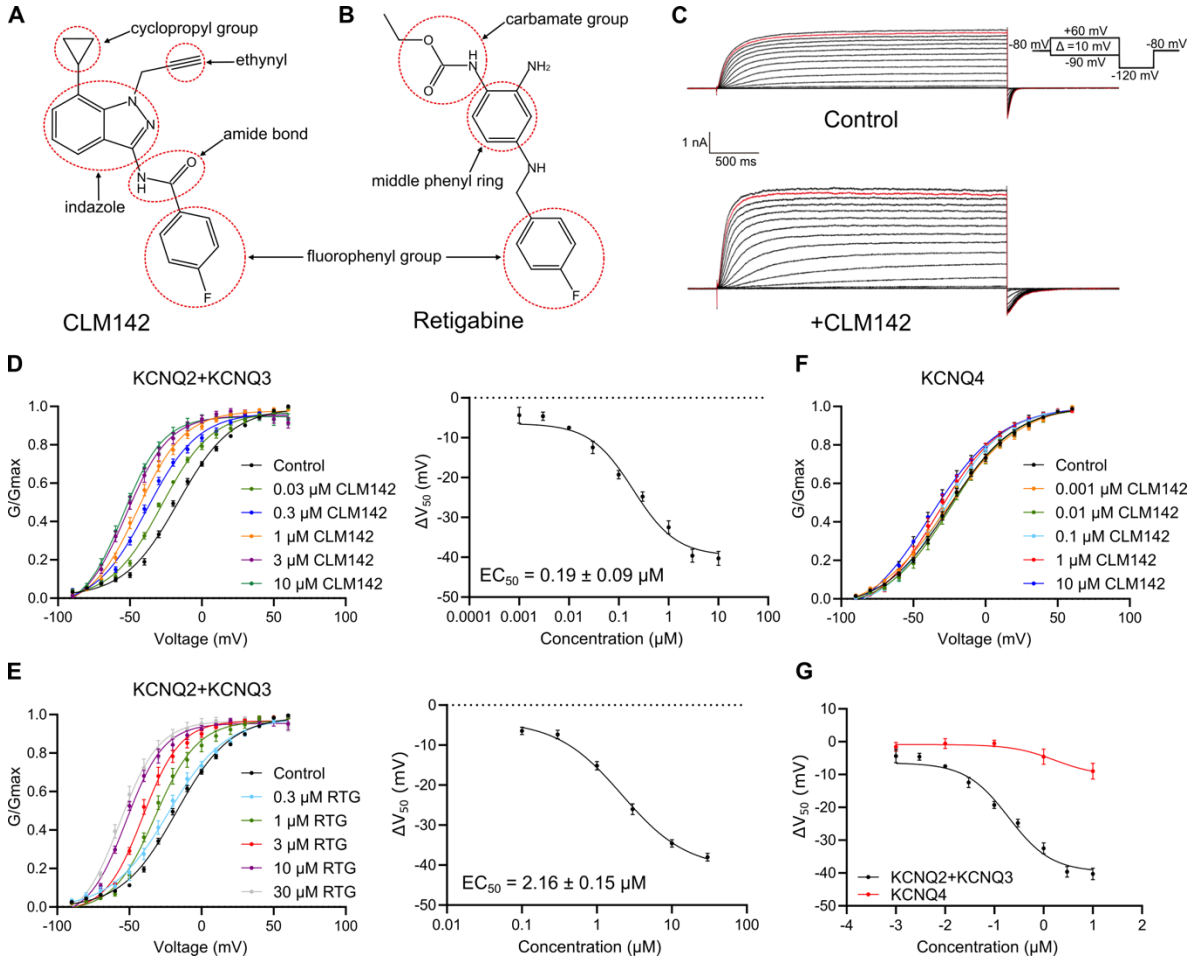

Figure 5

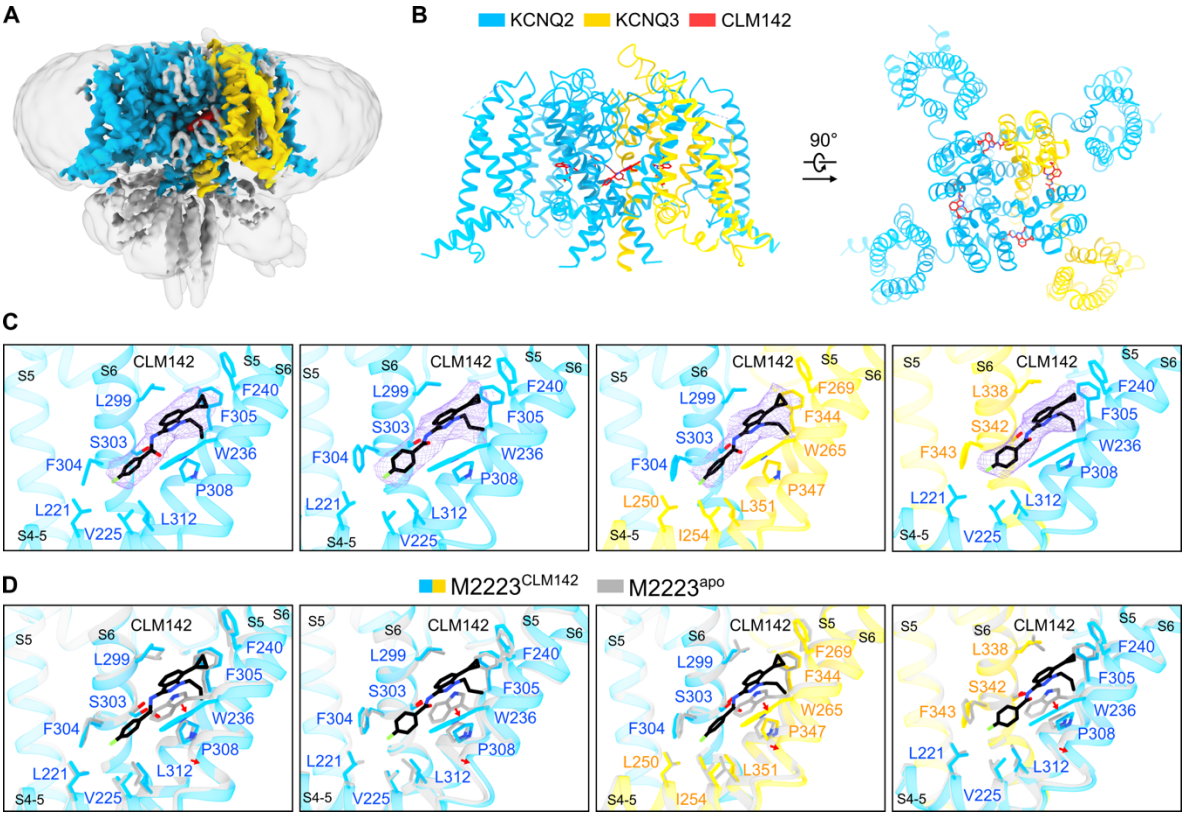

935 **Figure 6**

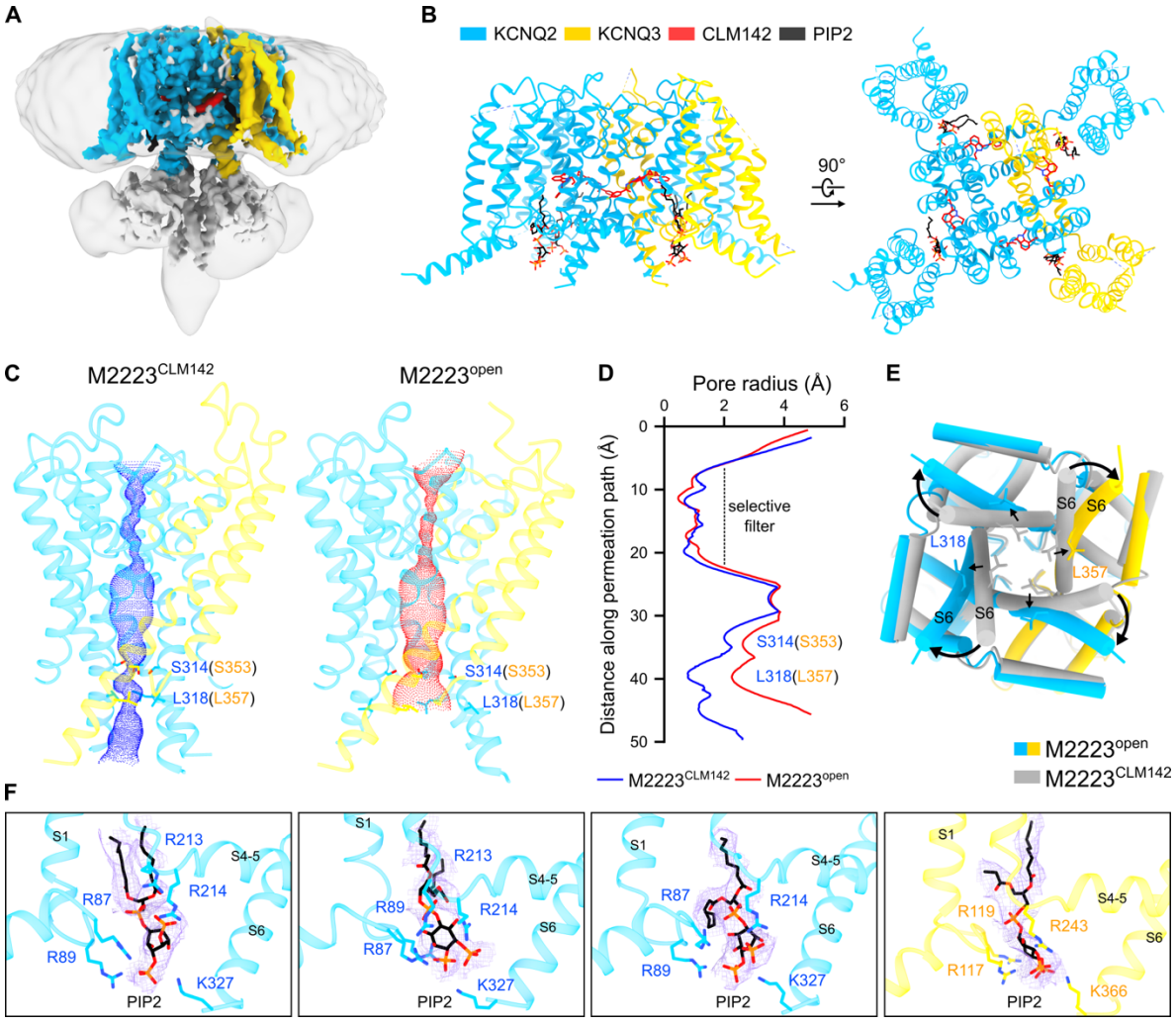

936

937

Supplementary Materials for

Structural basis for heteromeric assembly and subthreshold activation of human M-channel

Yifei Wang, Hui Yang, Yannan Qu , Junnan Li, Wenxin Hou, Kun Wu, Guanglei Xie, Xi Wang, Yangliang Ye, Huaiyu Yang, and Huaizong Shen

Correspondence to: H. Yang (hyyang@bio.ecnu.edu.cn); H. Shen (shenhuaizong@westlake.edu.cn).

This PDF file includes:

Figs. S1 to S17
Tables S1-S5
References and Notes

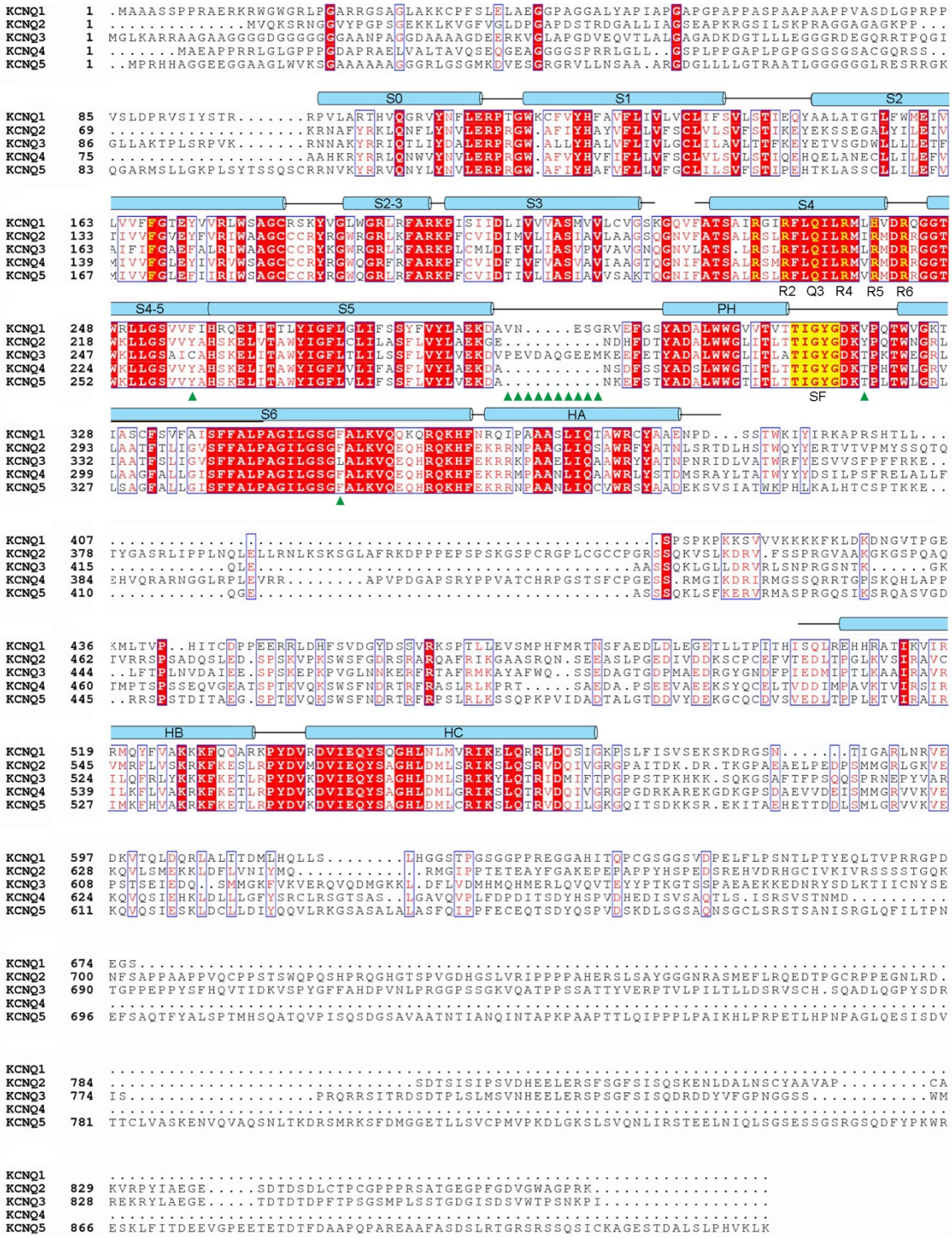

Fig. S1 | Sequence alignment of human KCNQ channels. Multiple sequence alignment of human KCNQ1 through KCNQ5, performed with Clustal Omega (*93*) and colored with ENDscript 2 (*94*). Invariant residues are shaded red, and conserved residues are printed in red. Key functional motifs are highlighted: residues forming the selectivity filter (SF) are shaded yellow and colored red; gating charge residues in the S4 helix and the F137/F167 residue (KCNQ2/KCNQ3 numbering) of the charge transfer center (CTC) are colored yellow. The extended extracellular loop between the S5 segment and the pore helix (PH) in KCNQ3, along with other key residues used for subtype discrimination between KCNQ2 and KCNQ3, are indicated with green triangles.

UniProt accession numbers: KCNQ1 (P51787), KCNQ2 (O43526), KCNQ3 (O43525), KCNQ4 (P56696), KCNQ5 (Q9NR82).

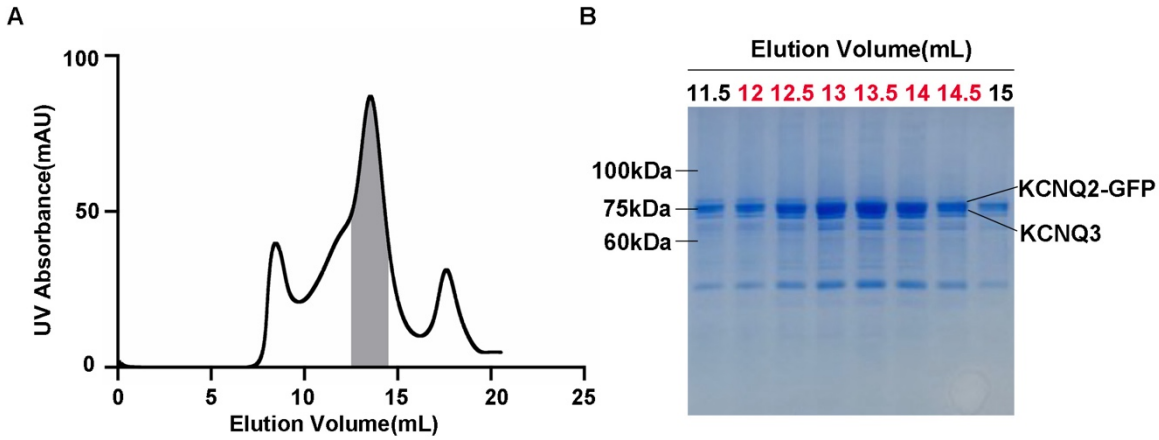

971

972 **Fig. S2 | Protein purification of human M-channel^{apo}.** (**A**) Representative size-exclusion

973 chromatography (SEC) profile of the heteromeric KCNQ2/3 (M-channel^{apo}) complex. (**B**)

974 SDS-PAGE analysis (Coomassie Brilliant Blue staining) of the peak fractions from the SEC

975 run. The fractions concentrated for cryo-EM grid preparation are indicated in red.

976

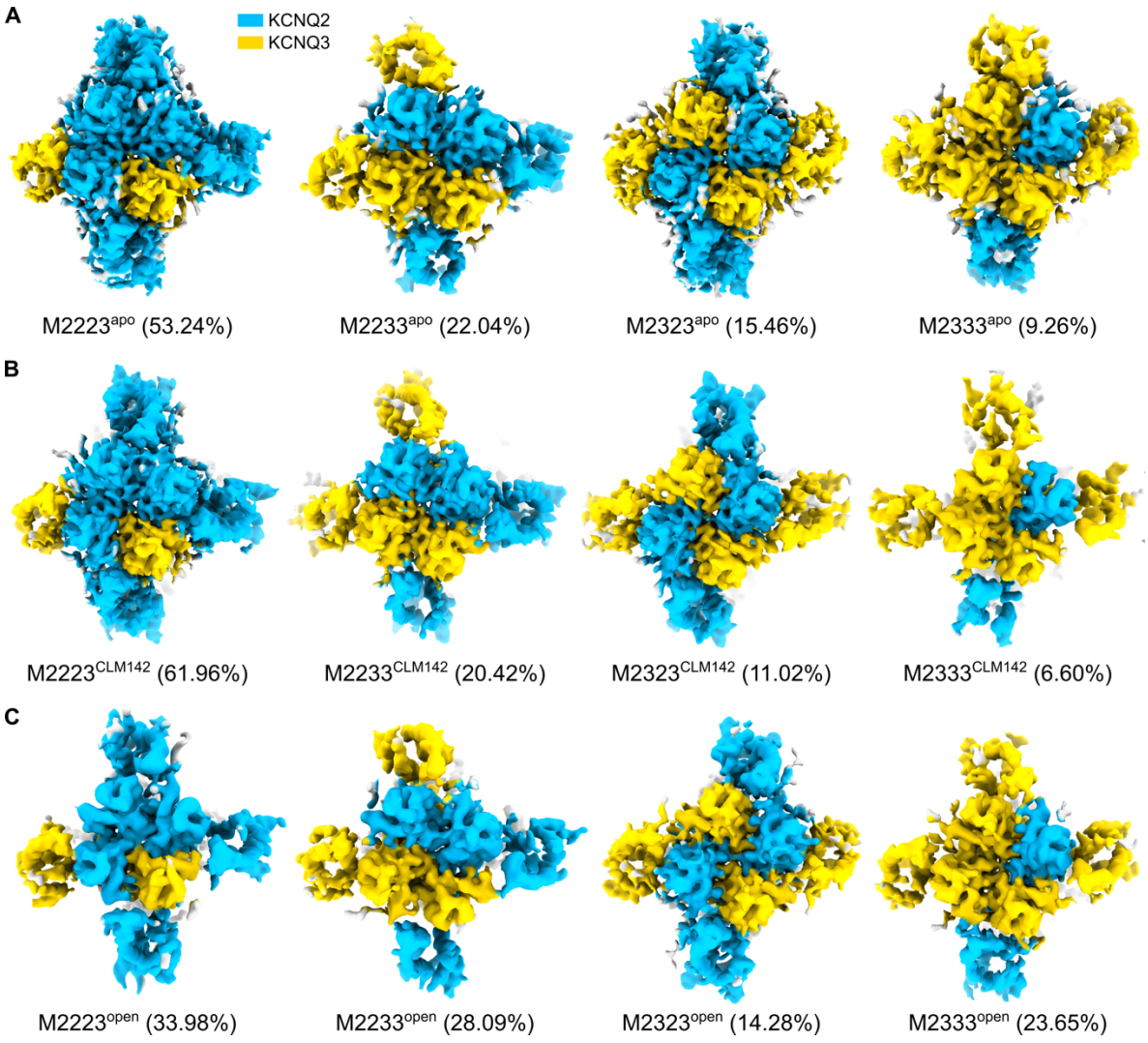

Fig. S3 | Cryo-EM reconstructions of M-channel in three functional states. (**A-C**) Cryo-EM reconstructions of the heteromeric KCNQ2/3 channel in the apo (**A**), CLM142-bound (**B**), and PIP_2-bound open (**C**) states. The relative proportions of the distinct stoichiometric assemblies (M2223, M2233, M2323, M2333) identified in each reconstruction are indicated. KCNQ2 and KCNQ3 subunits are colored blue and yellow, respectively.

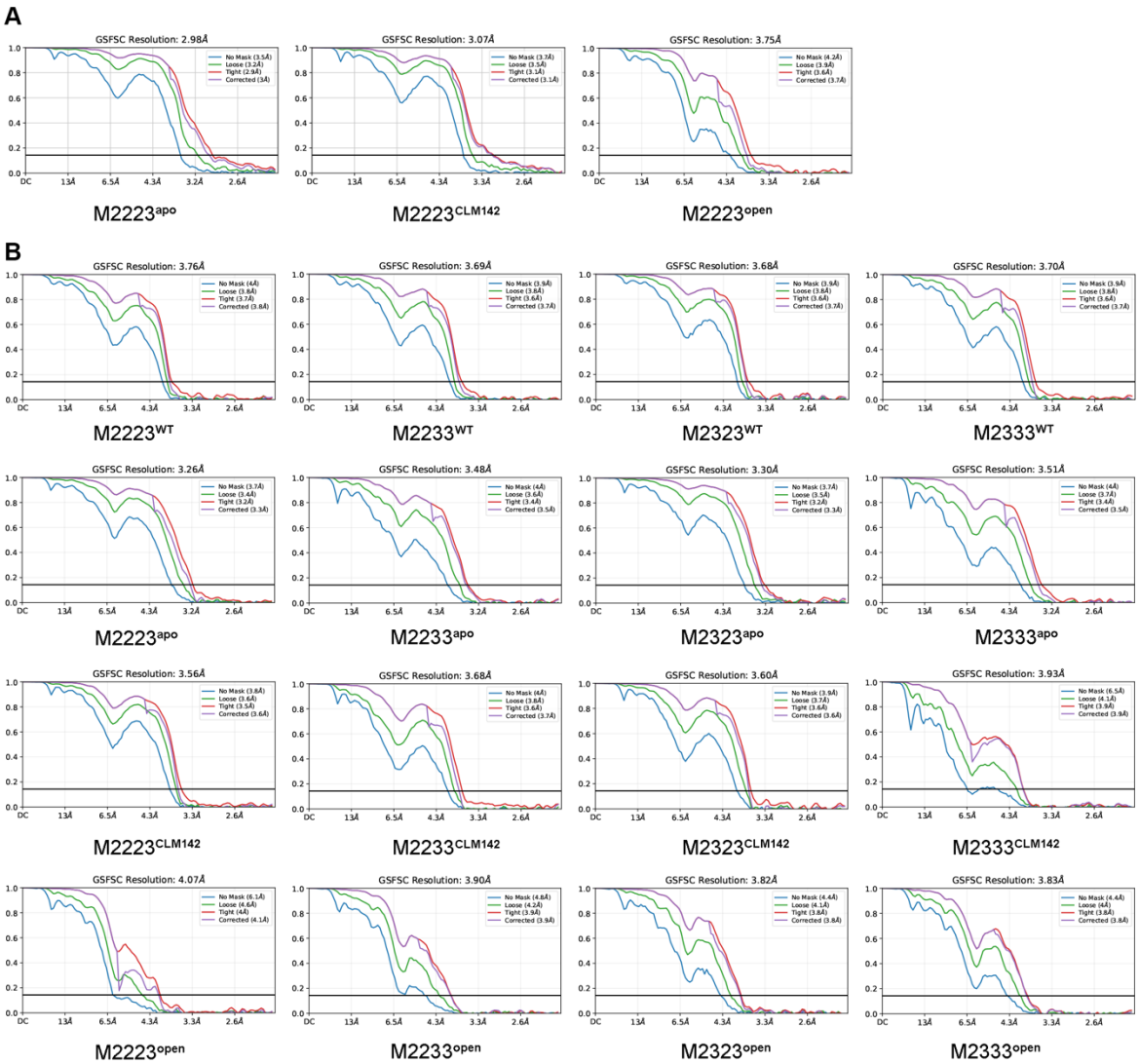

Fig. S4 | Fourier shell correlation (FSC) curves for M-channel reconstructions. (**A**) Gold-standard FSC curves for the M2223^{apo}, M2223^{CLM142}, and M2223^{open} reconstructions, determined without symmetry expansion. (**B**) FSC curves for all four different stoichiometric assemblies (M2223, M2233, M2323, M2333) reconstructions of M-channel^{WT}, M-channel^{apo}, M-channel^{CLM142}, and M-channel^{open}, determined using C4 symmetry expansion during processing.

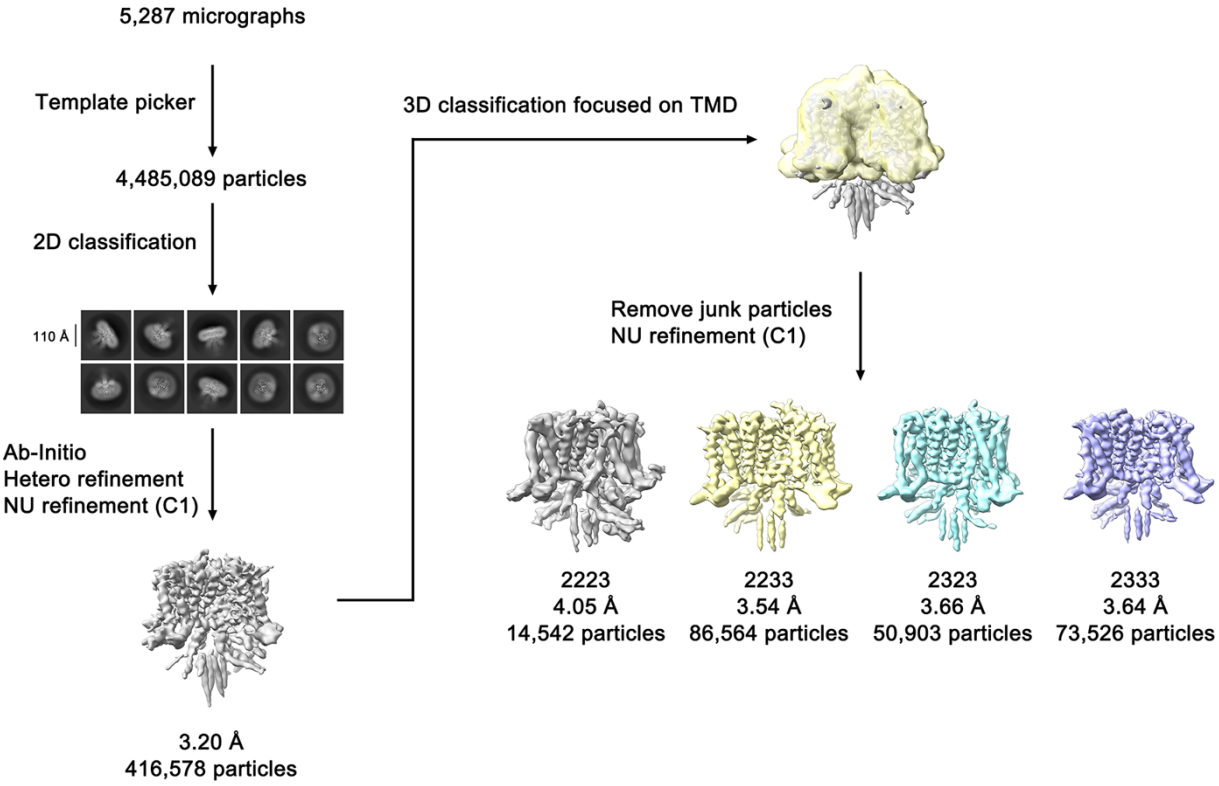

Fig. S5 | Cryo-EM data processing flowchart for M-channel^{WT}. Detailed flowchart of the cryo-EM data processing strategy for the wild-type M-channel reconstruction. Please refer to the "Cryo-EM data processing" section in MATERIALS AND METHODS for complete details.

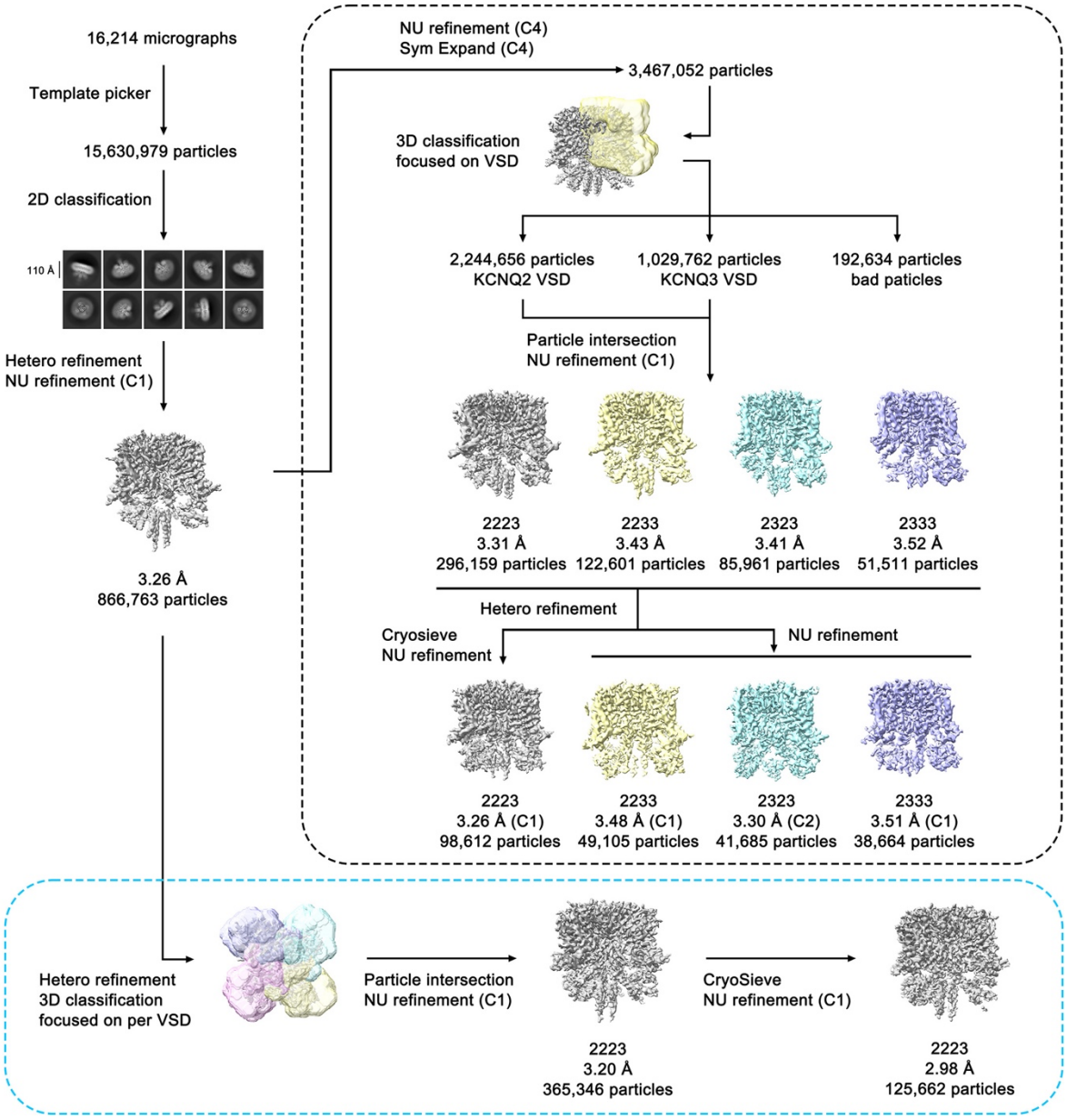

Fig. S6 | Cryo-EM data processing flowchart for M-channel^{apo}. Detailed flowchart of the cryo-EM data processing strategy for the M-channel^{apo} reconstruction. Please refer to the "Cryo-EM data processing" section in MATERIALS AND METHODS for complete details.

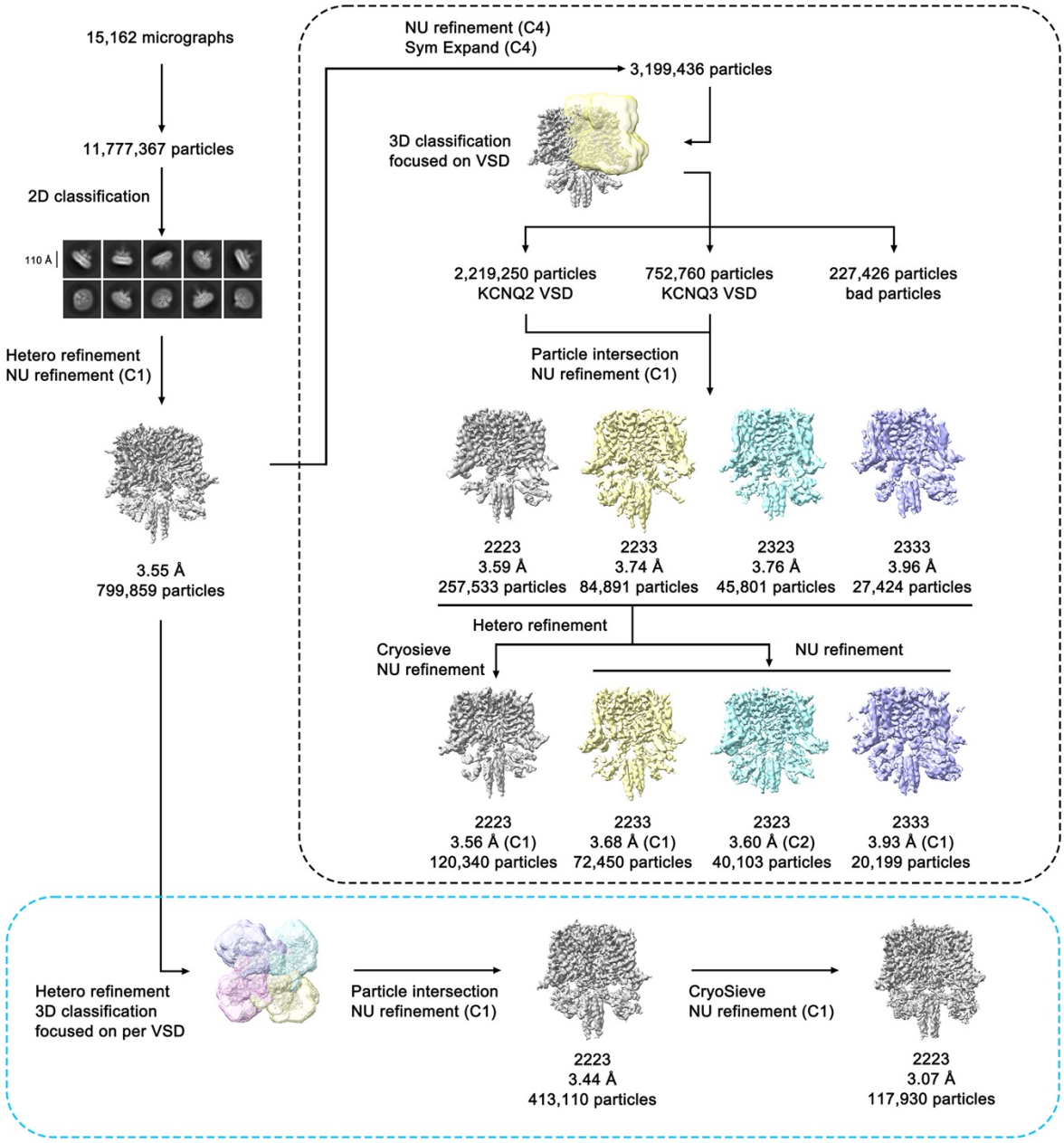

Fig. S7 | Cryo-EM data processing flowchart for M-channel^{CLM142}. Detailed flowchart of the cryo-EM data processing strategy for the M-channel^{CLM142} reconstruction. Please refer to the "Cryo-EM data processing" section in MATERIALS AND METHODS for complete details.

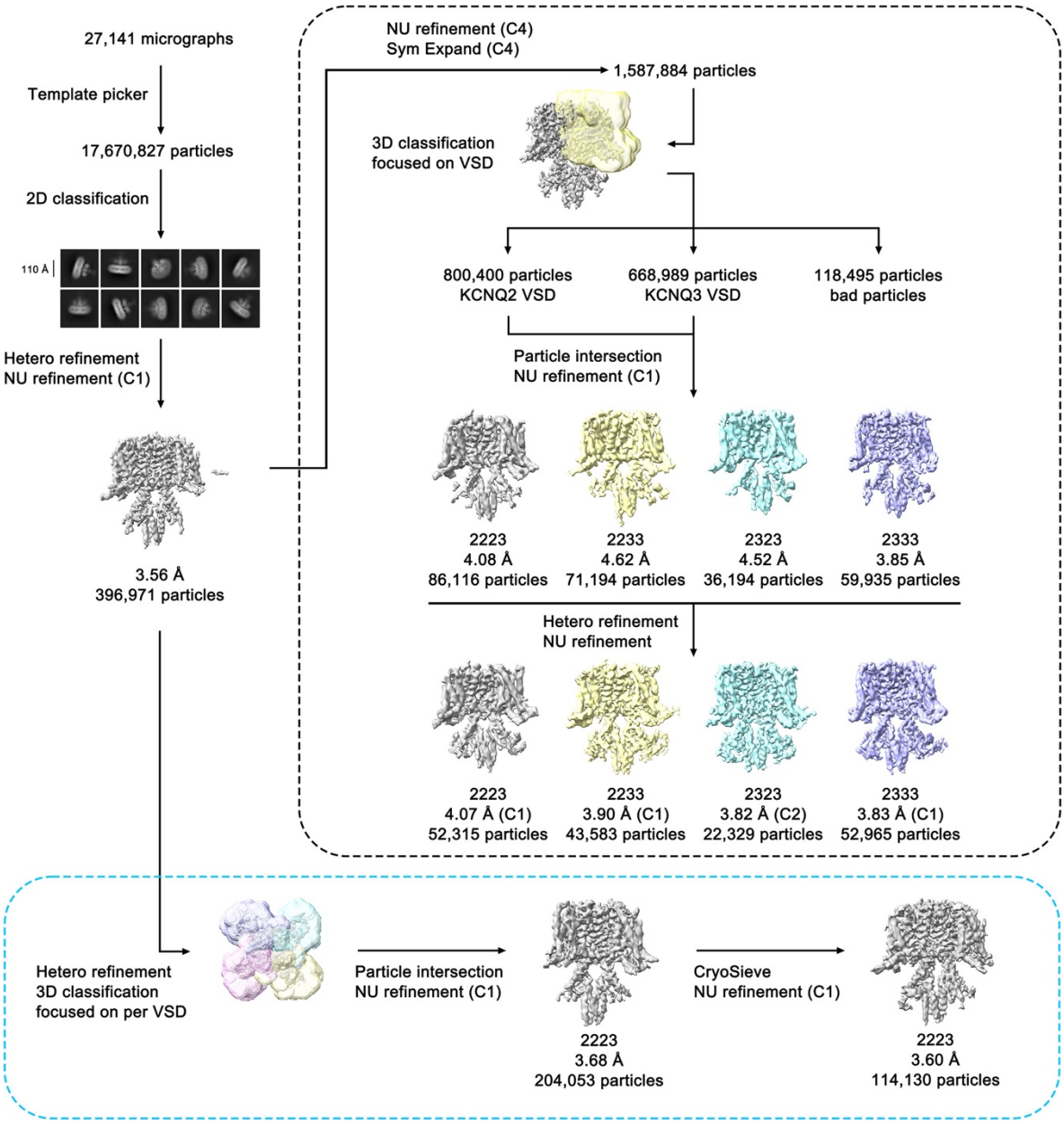

Fig. S8 | Cryo-EM data processing flowchart for M-channel^{open}. Detailed flowchart of the cryo-EM data processing strategy for the M-channel^{open} reconstruction. Please refer to the "Cryo-EM data processing" section in MATERIALS AND METHODS for complete details.

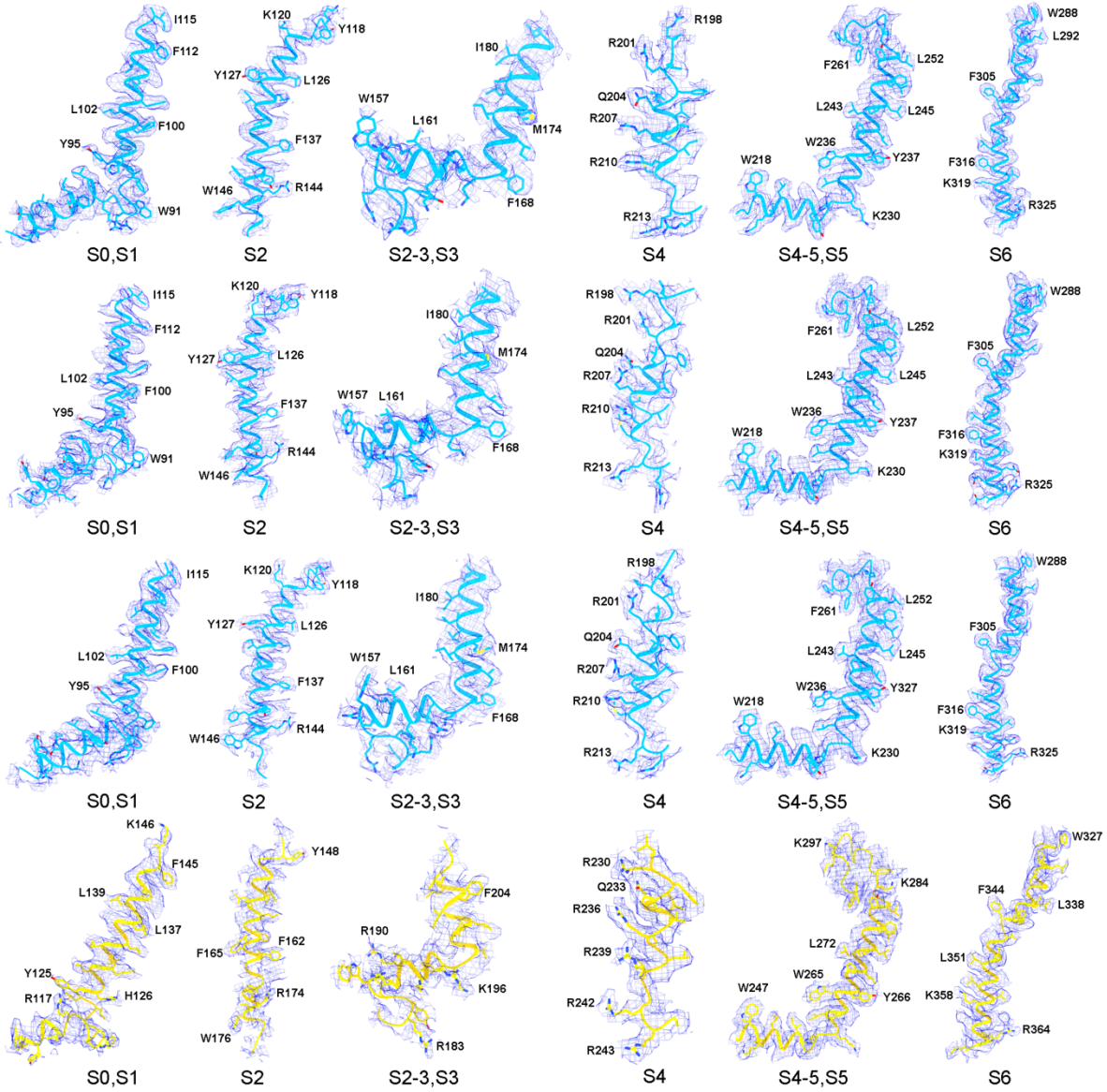

Fig. S9 | Cryo-EM densities of M2223^{apo}. Representative cryo-EM density maps for the M2223^{apo} atomic model, visualized in UCSF ChimeraX. Select residues with large side chains are labeled.

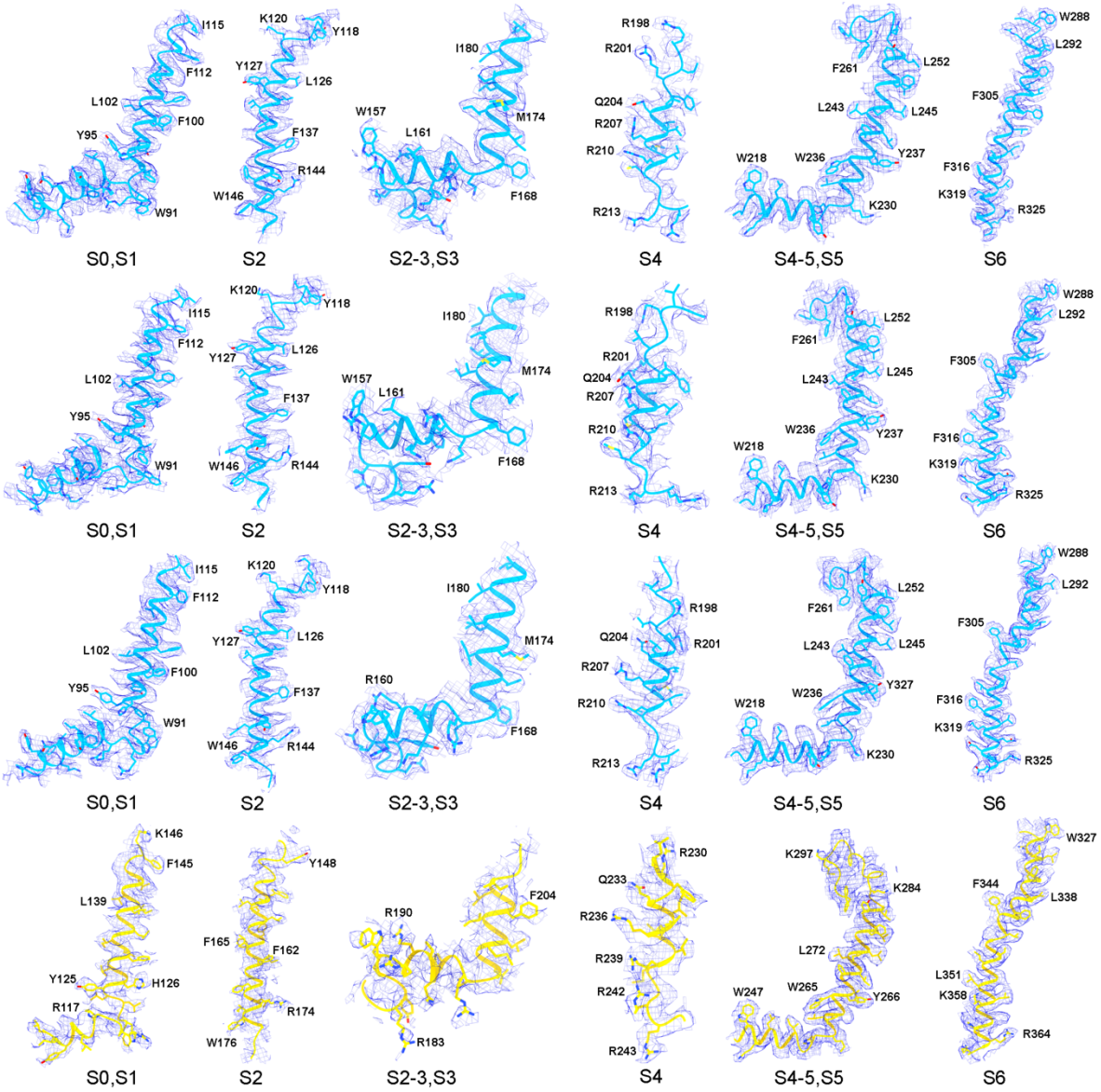

Fig. S10 | Cryo-EM densities of M2223^{CLM142}. Representative cryo-EM density maps for the M2223^{CLM142} atomic model, visualized in UCSF ChimeraX. Select residues with large side chains are labeled.

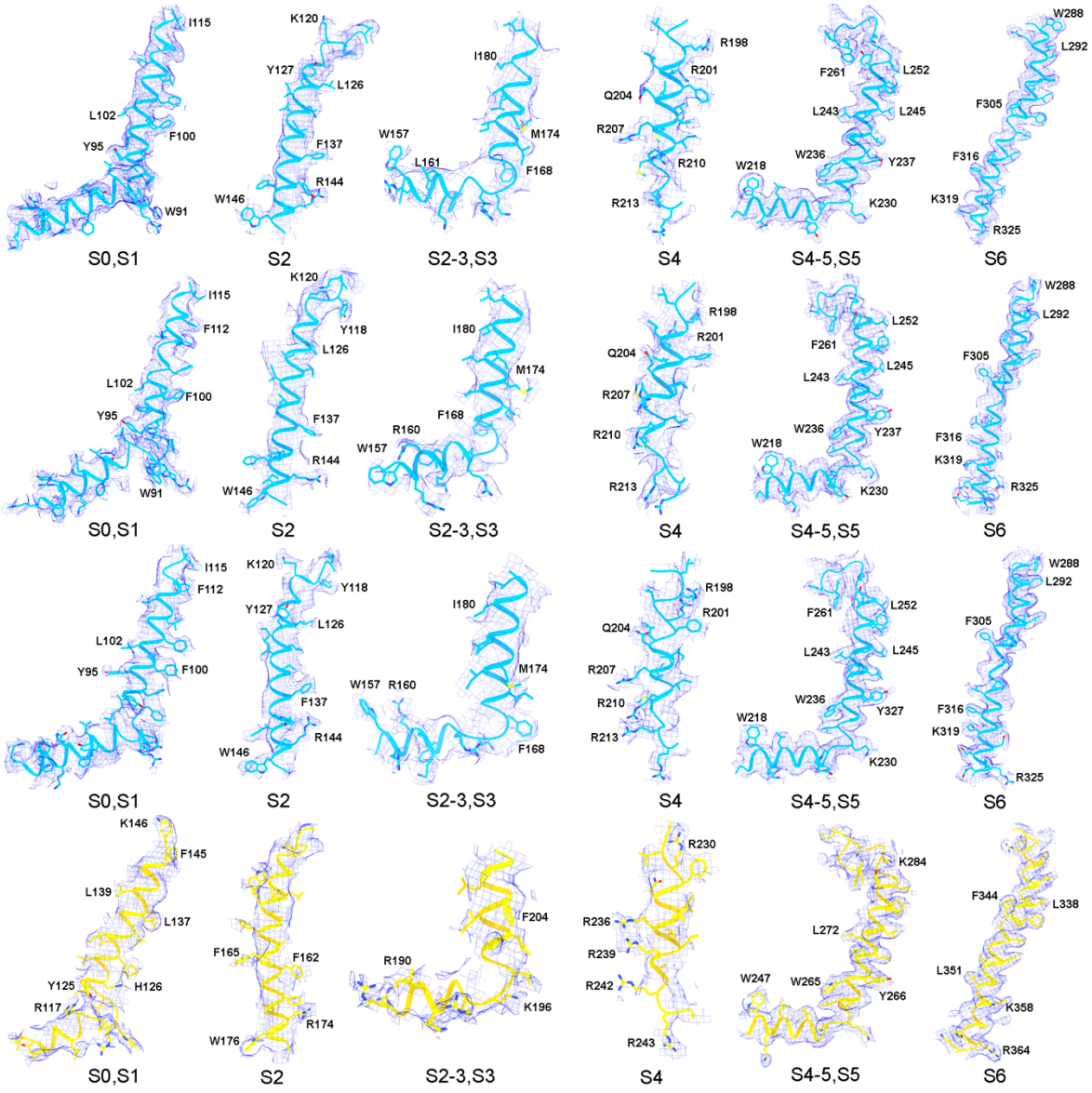

Fig. S11 | Cryo-EM densities of M2223^{open}. Representative cryo-EM density maps for the M2223^{open} atomic model, visualized in UCSF ChimeraX. Select residues with large side chains are labeled.

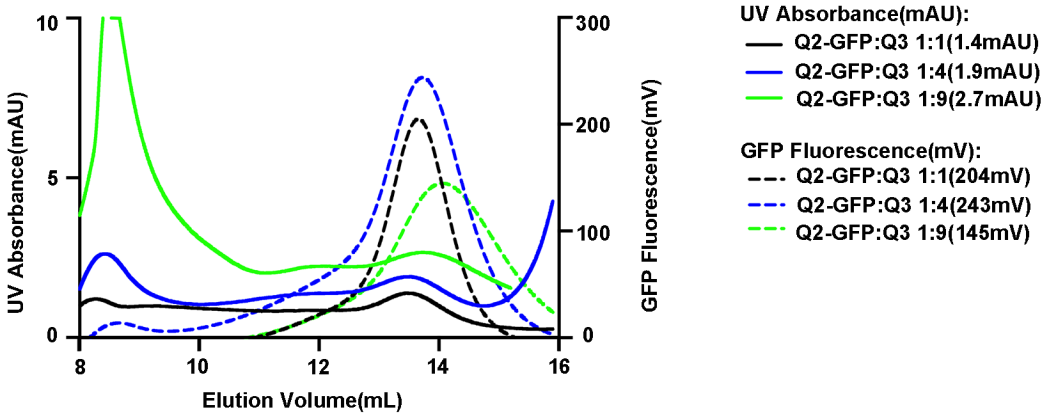

Fig. S12 | Expression and assembly of KCNQ2 and KCNQ3 at varying transfection ratios.

Size exclusion chromatography (SEC) profiles of heteromeric KCNQ2/KCNQ3 complexes co-expressed at 1:1 (black), 1:4 (blue), and 1:9 (green) transfection ratios, with the total plasmid amount kept constant (1.5 mg/L). Solid lines represent total protein UV absorbance; dashed lines correspond to GFP fluorescence (tagged on KCNQ2), indicating the relative amount of KCNQ2 incorporated into the complexes.

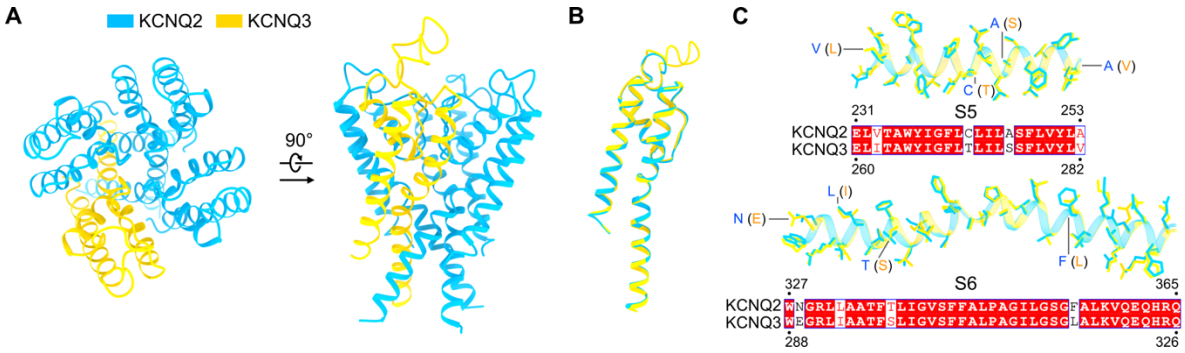

1039

1040 **Fig. S13 | Structural and sequence conservation of the pore domain in KCNQ2 and**

1041 **KCNQ3.** (**A**) Architecture of the pore domain in the M2223^{apo} structure, formed by the S5

1042 and S6 segments from three KCNQ2 subunits (blue) and one KCNQ3 subunit (yellow). (**B**)

1043 Structural superposition of the pore domains from KCNQ2 and KCNQ3, demonstrating

1044 high conformational similarity (RMSD = 0.437 Å). (**C**) Sequence alignment of the S5 and

1045 S6 segments between KCNQ2 and KCNQ3, highlighting strong conservation with >80%

1046 identity and >90% similarity.

1047

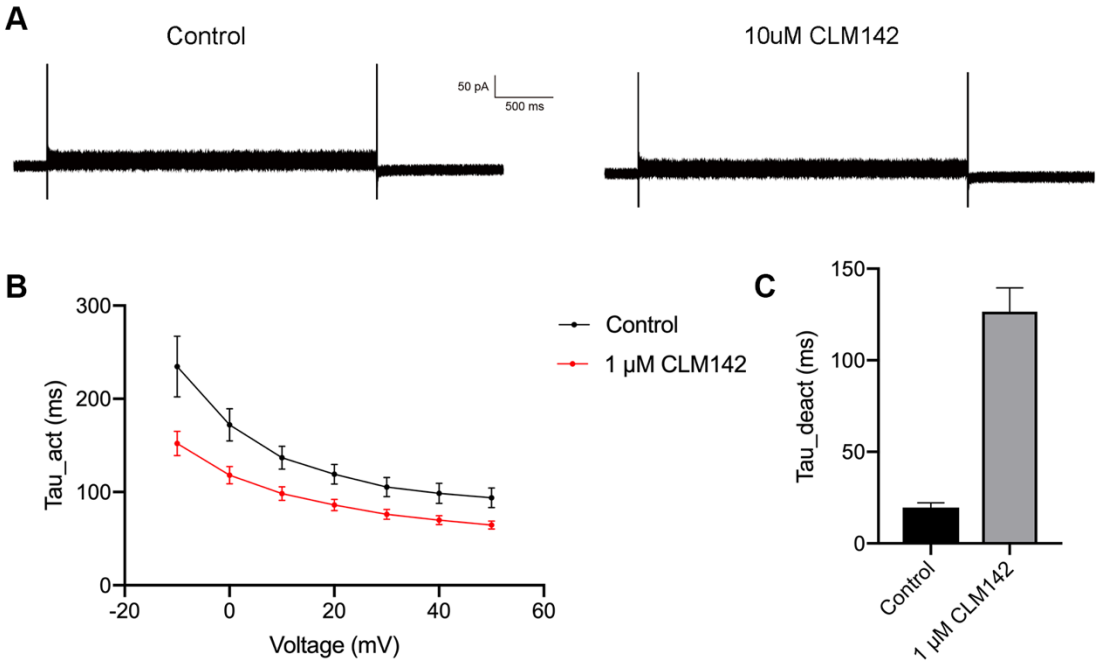

Fig. S14 | Functional characterization of CLM142 specificity and kinetics. (**A**) Whole-cell patch-clamp recordings from non-transfected cells before and after application of 10 μM CLM142, demonstrating the compound has no direct effect on endogenous currents. (**B**) Analysis of activation time constants (τ activation) for KCNQ2/KCNQ3 channels in the absence and presence of 1 μM CLM142. (**C**) Analysis of deactivation time constants (τ deactivation) for KCNQ2/KCNQ3 channels in the absence and presence of 1 μM CLM142. Data are presented as mean ± SEM.

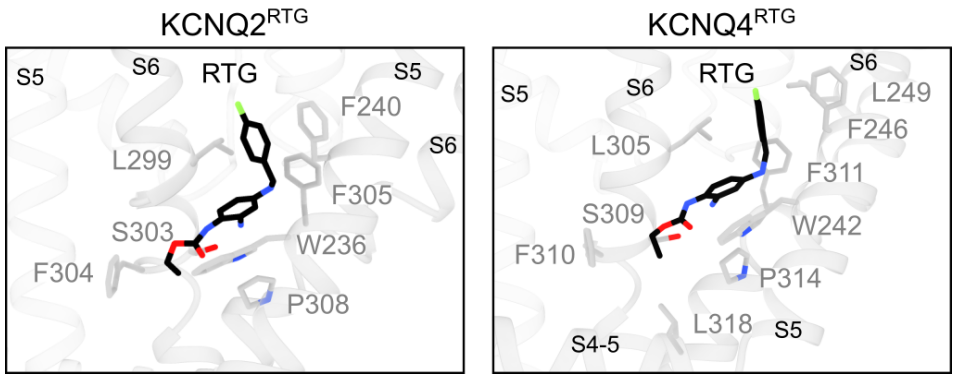

Fig. S15 | Retigabine binding in KCNQ2 and KCNQ4. (**A**) Molecular interactions between retigabine (black) and the pore domain of KCNQ2 (PDB: 7CR2),(*39*) with key coordinating residues shown as sticks. (**B**) Molecular interactions between retigabine (black) and the pore domain of KCNQ4 (PDB: 7BYM),(*45*) with key coordinating residues shown as sticks.

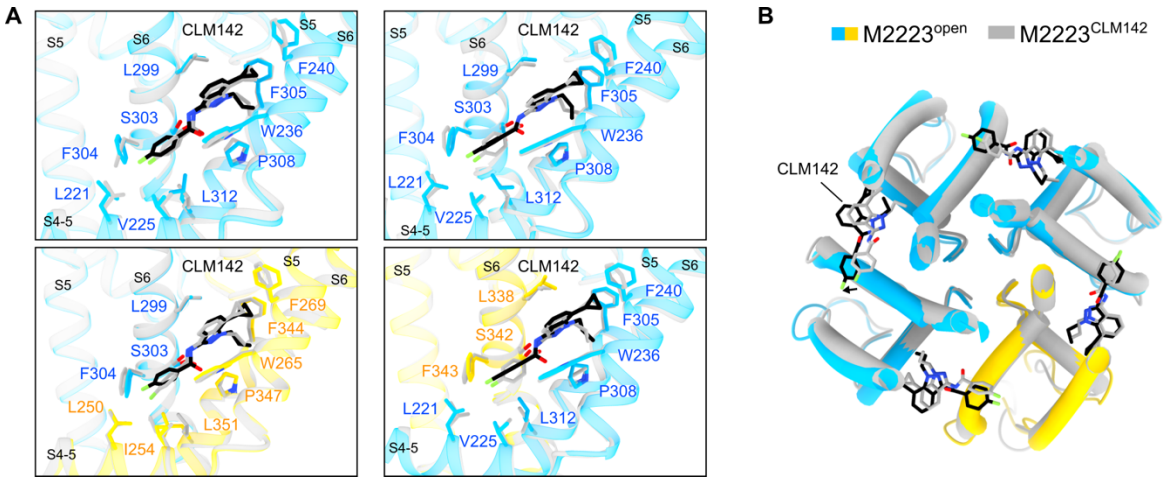

Fig. S16 | Structural comparison of M2223^{CLM142} and M2223^{open}. (**A**) Structural alignment of the M2223^{CLM142} and M2223^{open} complexes reveals subtle conformational changes. While the four bound CLM142 molecules undergo slight positional shifts, their key interacting residues in KCNQ2 and KCNQ3 remain largely unchanged. (**B**) Intracellular view of the activation-associated structural transitions of the pore domain, highlighting the displacement of the CLM142 molecules during pore opening.

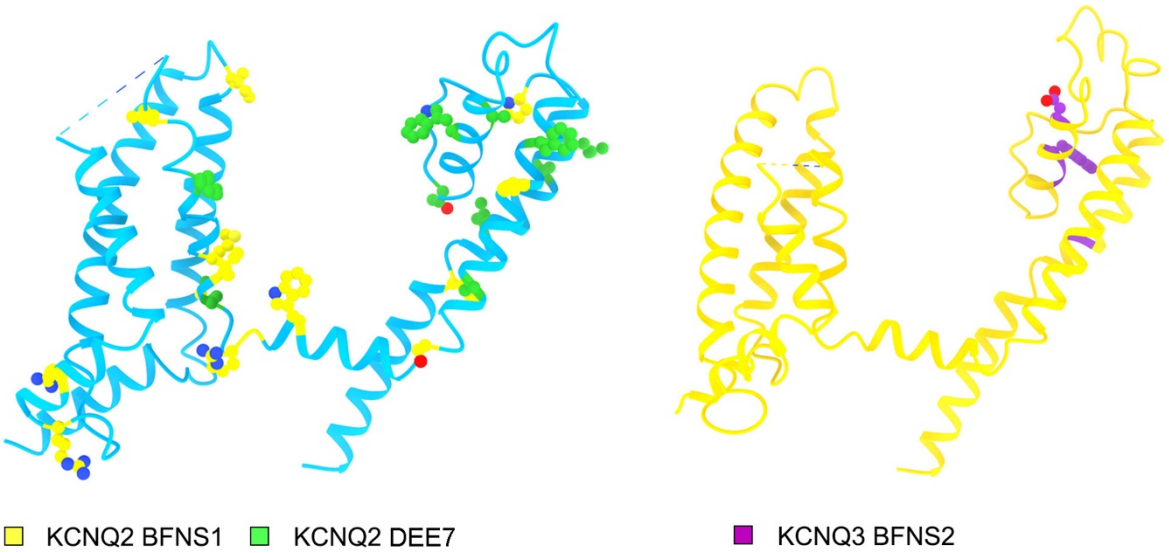

Fig. S17 | Structural mapping of M-channel diesease mutations. Structural mapping of disease-related mutations in human KCNQ2 and KCNQ3 subunits. Mutations associated with Benign Familial Neonatal Seizures 1 (BFNS1) and Developmental and Epileptic Encephalopathy 7 (DEE7) in KCNQ2, and Benign Familial Neonatal Seizures 2 (BFNS2) in KCNQ3, are highlighted on the M-channel structure.

Table S1 | Statistics for data collection and structural refinement for M2223^{apo}, M2223^{CLM142}, and M2223^{open} determined without using symmetry expansion.

Data collection	M2223^{apo}	M2223^{CLM142}	M2223^{open}
EM equipment	Titan Krios (Thermo Fisher Scientific Inc.)		
Voltage (kV)	300		
Detector	Gatan K3 Summit		
Energy filter	Gatan GIF Quantum, 20 eV slit		
Pixel size (Å)	1.0773	1.087	1.087
Electron dose (e^-/Å^2)	50		
Defocus range (μm)	-1.5 ~ -2.0		
Number of collected movie stacks	16,214	15,162	27,141
Reconstruction			
Software	CryoSPARC v4		
Number of used particles	125,662	117,930	85,732
Symmetry	C1	C1	C1
Overall resolution (Å)	2.98	3.07	3.75
Map sharpening B-factor (Å^2)	126.1	131.7	157.7
Refinement			
Software	Phenix		
Cell dimensions			
a=b=c (Å)	258.552	260.88	260.88
α=β=γ (˚)	90	90	90
Model composition			
Protein residues	975	975	938
Side chains assigned	975	975	938
Ligands	GDN: 3 9PE: 3	LIG: 4 GDN: 3 9PE: 3	LIG: 4 PIO: 3
R.m.s deviations			
Bonds length (Å)	0.004	0.003	0.006
Bonds angle (˚)	0.946	0.731	0.952
Ramachandran plot statistics (%)			
Preferred	93.12%	93.01%	92.21%
Allowed	6.47%	6.78%	7.13%
Outlier	0.42%	0.21%	0.66%

Table S2 | Statistics for data collection and structural refinement for M-channel^{WT} determined using C4 symmetry expansion.

Data collection	M2223^{WT}	M2233^{WT}	M2323^{WT}	M2333^{WT}
EM equipment	Titan Krios (Thermo Fisher Scientific Inc.)			
Voltage (kV)	300			
Detector	Gatan K3 Summit			
Energy filter	Gatan GIF Quantum, 20 eV slit			
Pixel size (Å)	1.087			
Electron dose (e^-/Å^2)	50			
Defocus range (μm)	-1.5 ~ -2.0			
Number of collected movie stacks	5,393			
Reconstruction				
Software	CryoSPARC v4			
Number of used particles	102,370	80,651	47,614	74,317
Symmetry	C1	C1	C2	C1
Overall resolution (Å)	3.76	3.69	3.75	3.70
Map sharpening B-factor (Å^2)	129.3	134.8	137.8	122.8
Refinement				
Software	Phenix			
Cell dimensions				
a=b=c (Å)	260.88			
α=β=γ (˚)	90			
Model composition				
Protein residues	975	971	968	964
Side chains assigned	975	971	968	964
Ligands	GDN: 3 9PE: 3	GDN: 2 9PE: 2	GDN: 2 9PE: 2	GDN: 1 9PE: 1
R.m.s deviations				
Bonds length (Å)	0.003	0.003	0.003	0.004
Bonds angle (˚)	0.763	0.730	0.694	0.753
Ramachandran plot statistics (%)				
Preferred	93.01%	93.19%	92.33%	91.67%
Allowed	6.78%	6.81%	7.56%	8.02%
Outlier	0.21%	0.00%	0.11%	0.32%

Table S3 | Statistics for data collection and structural refinement for M-channel^{apo} determined using symmetry expansion.

Data collection	M2223^{apo}	M2233^{apo}	M2323^{apo}	M2333^{apo}
EM equipment	Titan Krios (Thermo Fisher Scientific Inc.)			
Voltage (kV)	300			
Detector	Gatan K3 Summit			
Energy filter	Gatan GIF Quantum, 20 eV slit			
Pixel size (Å)	1.0773			
Electron dose (e^-/Å^2)	50			
Defocus range (μm)	-1.5 ~ -2.0			
Number of collected movie stacks	16,214			
Reconstruction				
Software	CryoSPARC v4			
Number of used particles	98,612	49,105	41,685	38,664
Symmetry	C1	C1	C2	C1
Overall resolution (Å)	3.26	3.48	3.30	3.51
Map sharpening B-factor (Å^2)	128.0	124.1	132.0	119.5
Refinement				
Software	Phenix			
Cell dimensions				
a=b=c (Å)	258.552			
α=β=γ (˚)	90			
Model composition				
Protein residues	975	971	968	964
Side chains assigned	975	971	968	964
Ligands	GDN: 3 9PE: 3	GDN: 2 9PE: 2	GDN: 2 9PE: 2	GDN: 1 9PE: 1
R.m.s deviations				
Bonds length (Å)	0.003	0.003	0.003	0.004
Bonds angle (˚)	0.657	0.745	0.896	0.729
Ramachandran plot statistics (%)				
Preferred	93.85%	93.09%	92.44%	92.62%
Allowed	5.94%	6.81%	7.25%	6.96%
Outlier	0.21%	0.10%	0.32%	0.42%

Table S4 | Statistics for data collection and structural refinement for M-channel^{CLM142} determined using symmetry expansion.

Data collection	M2223^{CLM142}	M2233^{CLM142}	M2323^{CLM142}	M2333^{CLM142}
EM equipment	Titan Krios (Thermo Fisher Scientific Inc.)			
Voltage (kV)	300			
Detector	Gatan K3 Summit			
Energy filter	Gatan GIF Quantum, 20 eV slit			
Pixel size (Å)	1.087			
Electron dose (e^-/Å^2)	50			
Defocus range (μm)	-1.5 ~ -2.0			
Number of collected movie stacks	15,162			
Reconstruction				
Software	CryoSPARC v4			
Number of used particles	120,340	72,450	40,103	20,199
Symmetry	C1	C1	C2	C1
Overall resolution (Å)	3.56	3.68	3.60	3.93
Map sharpening B-factor (Å^2)	123.8	126.2	123.2	105.5
Refinement				
Software	Phenix			
Cell dimensions				
a=b=c (Å)	260.88			
α=β=γ (˚)	90			
Model composition				
Protein residues	975	971	968	964
Side chains assigned	975	971	968	964
Ligands	LIG: 4 GDN: 3 9PE: 3	LIG: 4 GDN: 2 9PE: 2	LIG: 4 GDN: 2 9PE: 2	LIG: 4 GDN: 1 9PE: 1
R.m.s deviations				
Bonds length (Å)	0.003	0.004	0.003	0.006
Bonds angle (˚)	0.719	0.836	0.796	1.012
Ramachandran plot statistics (%)				
Preferred	94.06%	92.46%	93.28%	91.56%
Allowed	5.74%	7.23%	6.62%	8.33%
Outlier	0.21%	0.31%	0.11%	0.11%

Table S5 | Statistics for data collection and structural refinement for M-channel^{open} determined using symmetry expansion.

Data collection	M2223^{open}	M2233^{open}	M2323^{open}	M2333^{open}
EM equipment	Titan Krios (Thermo Fisher Scientific Inc.)			
Voltage (kV)	300			
Detector	Gatan K3 Summit			
Energy filter	Gatan GIF Quantum, 20 eV slit			
Pixel size (Å)	1.087			
Electron dose (e^-/Å^2)	50			
Defocus range (μm)	-1.5 ~ -2.0			
Number of collected movie stacks	27,141			
Reconstruction				
Software	CryoSPARC v4			
Number of used particles	52,315	43,583	22,329	52,965
Symmetry	C1	C1	C2	C1
Overall resolution (Å)	4.07	3.90	3.82	3.83
Map sharpening B-factor (Å^2)	181.6	149.5	141.2	141.1
Refinement				
Software	Phenix			
Cell dimensions				
a=b=c (Å)	260.88			
α=β=γ (˚)	90			
Model composition				
Protein residues	938	920	920	902
Side chains assigned	938	920	920	902
Ligands	LIG: 4 PIO: 3	LIG: 4 PIO: 2	LIG: 4 PIO: 2	LIG: 4 PIO: 1
R.m.s deviations				
Bonds length (Å)	0.003	0.004	0.004	0.004
Bonds angle (˚)	0.810	0.937	0.867	0.859
Ramachandran plot statistics (%)				
Preferred	93.75%	92.60%	93.83%	93.46%
Allowed	5.81%	6.95%	5.49%	5.96%
Outlier	0.44%	0.45%	0.67%	0.57%